AD A111910

NRL Memorandum Report 4753

Multi-Component Model of the Resistive Hose Instability

WILLIAM M. SHARP

Science Applications, Inc.
McLean, VA 22102

MARTIN LAMPE

Plasma Theory Branch
Plasma Physics Division

HAN S. UHM

Naval Surface Weapons Center
Silver Spring, MD 20910

March 4, 1982

This work was sponsored by the Defense Advanced Research Projects Agency (DoD)
under ARPA Order No. 4395, Amendment No. 1.

NAVAL RESEARCH LABORATORY
Washington, D.C.

Approved for public release; distribution unlimited.

DTIC FILE COPY

DTIC
ELECTE
MAR 1 1 1982
S D

82 03 11 126

A

SECURITY CLASSIFICATION OF THIS PAGE (When Data Entered)

REPORT DOCUMENTATION PAGE	READ INSTRUCTIONS BEFORE COMPLETING FORM
1. REPORT NUMBER: NRL Memorandum Report 4753 — 2. GOVT ACCESSION NO.: AD-A111 910	3. RECIPIENT'S CATALOG NUMBER
4. TITLE (and Subtitle): MULTI-COMPONENT MODEL OF THE RESISTIVE HOSE INSTABILITY	5. TYPE OF REPORT & PERIOD COVERED: Interim report on a continuing NRL problem.
	6. PERFORMING ORG. REPORT NUMBER
7. AUTHOR(s): William M. Sharp*, Martin Lampe, and Han S. Uhm**	8. CONTRACT OR GRANT NUMBER(s)
9. PERFORMING ORGANIZATION NAME AND ADDRESS: Naval Research Laboratory, Washington, DC 20375	10. PROGRAM ELEMENT, PROJECT, TASK AREA & WORK UNIT NUMBERS: 47-0900-0-2
11. CONTROLLING OFFICE NAME AND ADDRESS: Defense Advanced Research Projects Agency, Arlington, VA 22209	12. REPORT DATE: March 4, 1982
	13. NUMBER OF PAGES: 69
14. MONITORING AGENCY NAME & ADDRESS(if different from Controlling Office)	15. SECURITY CLASS. (of this report): UNCLASSIFIED
	15a. DECLASSIFICATION/DOWNGRADING SCHEDULE

16. DISTRIBUTION STATEMENT (of this Report)

Approved for public release; distribution unlimited.

17. DISTRIBUTION STATEMENT (of the abstract entered in Block 20, if different from Report)

18. SUPPLEMENTARY NOTES

*Present address: Science Applications, Inc., McLean, VA 22102
**Present address: Naval Surface Weapons Center, Silver Spring, MD 20910
This work was sponsored by the Defense Advanced Research Projects Agency (DoD) under ARPA Order No. 4395, Amendment No. 1.

19. KEY WORDS (Continue on reverse side if necessary and identify by block number)

Beam propagation
Hose instability
Heavy ion fusion
Plasma instabilities
Relativistic electron beams
Bounce-resonance instabilities

20. ABSTRACT (Continue on reverse side if necessary and identify by block number)

A new model of beam dynamics is presented for treating the resistive hose instability in intense, self-pinched electron or ion beams. The beam is modeled as a superposition of rigid, independently-moving components with different radii. This multi-component model exhibits the localized resonances and other analytic properties of a Vlasov treatment. The new model is used to calculate the eigenfunctions and the dispersion relation

(Continues)

DD FORM 1 JAN 73 1473 EDITION OF 1 NOV 65 IS OBSOLETE
S/N 0102-014-6601

SECURITY CLASSIFICATION OF THIS PAGE (When Data Entered)

20. ABSTRACT (Continued)

for hose instability of an axially uniform beam propagating in a medium of specified conductivity profile with any specified return current. Wave growth is found to be significantly increased by return current or by a narrow conductivity profile. The results are compared to those of earlier models.

CONTENTS

I. INTRODUCTION 1

II. HOSE EIGENVALUE PROBLEM 3

III. MULTI-COMPONENT FORMALISM 18

IV. RESULTS 29

ACKNOWLEDGMENTS 44

APPENDIX A — PARTICLE ORBIT PROPERTIES 45

APPENDIX B — EVALUATION OF THE VLASOV TIME INTEGRAL 55

REFERENCES 60

DTIC COPY INSPECTED 2

Accession For
NTIS GRA&I
DTIC TAB
Unannounced
Justification
By
Distribution/
Availability Codes
Dist | Avail and/or Special
A

MULTI-COMPONENT MODEL OF THE RESISTIVE HOSE INSTABILITY

I. Introduction

The resistive hose instability is a growing lateral distortion of an energetic self-pinched beam propagating in a dense resistive plasma. When there is no significant equilibrium return current, the instability is driven by a resistive lag of the magnetic field in responding to transverse displacements of the beam. The presence of return current further destabilizes the beam by magnetically repelling the displaced beam from the axis.

Although the hose instability has been studied extensively[1-8], most previous theoretical work is based on oversimplified models of beam particle dynamics. Since the pinch force is anharmonic whenever the radial profile of current density is rounded, particles have a spread of betatron frequencies that introduces phase mixing and tends to damp hose oscillations. In addition, the betatron frequency of a particle depends on the extent and shape of its orbit, leading to radially localized wave-particle resonances. The early rigid beam hose models[1,2] and kinetic treatments assuming helical particle orbits[3,4] omitted phase mixing entirely, and as a result, these models overestimated the degree of instability. The "spread-mass" model of Lee[5] was a significant improvement; by introducing a realistic amount of phase mixing in an artificial way, it gave a reasonable hose growth spectrum, even though the model neglected the correlation between the betatron frequency of particles and their radial location.

Recently, Uhm and Lampe[6] developed an "energy-group" model that exhibits radially localized resonances as well as phase mixing, and here we present an improved and refined version of that model. As in the Uhm-Lampe model, each beam slice is represented by a superposition of rigid

Manuscript submitted December 17, 1981.

components with different outer radii, each of which responds independently to the resultant transverse force acting on it. Since the beam response depends sensitively on the radial density profile of components, we use a Vlasov analysis here to guide the choice of component profiles. With an appropriate component shape, this "multi-component" beam dynamics model accurately reproduces the localized resonances and other analytic properties of a full Vlasov treatment, while still being tractable by straightforward numerical methods.

The outline of the paper is as follows. In Sec. II, we formulate the Vlasov eigenvalue problem for the hose instability and determine the analytic properties of the perturbed current $\hat{J}(r)$. The details are given in Appendices A and B. In Sec. III, we use the multi-component model to obtain an expression for $\hat{J}(r)$ and show that this form preserves the important analytic properties of the Vlasov result. The method of numerical solution for the dispersion relation and eigenfunctions is then outlined. The results of extensive numerical calculations are given in Sec. IV. We compare hose eigenfunctions and growth rates to earlier models and discuss the sensitivity of the growth rates to the equilibrium return current fraction and the radial profile of conductivity. Finally, we mention work in progress that extends the range of applicability of the model.

II. Hose Eigenvalue Problem

A. Assumptions and Basic Equations

The equilibrium considered here is an axisymmetric self-pinched beam of relativistic electrons moving in the positive z direction, with no bulk rotation or externally-imposed fields. We make the "paraxial" assumption that the transverse velocity of beam particles is small compared with the parallel velocity v_z. This assumption requires that $|I_n| \ll I_A$, where the net current I_n is the sum of the beam current I_b and plasma current I_p, and I_A is the Alfven-Lawson current, given in cgs units by $I_A \equiv (\gamma^2-1)^{1/2} Mc^3 |q|^{-1}$. Here, M is the mass of beam particles, q is the charge, and γ is the typical relativistic factor. It follows that the beam radius a is small compared with the betatron wavelength of beam particles $\lambda_\beta = \pi a (2I_A/|I_n|)^{1/2}$. The background gas is taken to be a stationary medium characterized by a conductivity $\sigma(r)$ large enough to provide space charge neutrality, which requires that $c/(4\pi\sigma) \ll a$. The effects of collisions between beam particles and background gas particles are ignored.

In the high-conductivity regime considered here, a non-rotating beam has only an axial vector potential component A_z, and all beam fields can be derived from it:

$$B_\theta = - \partial A_z/\partial r, \tag{1a}$$

$$B_r = r^{-1} \partial A_z/\partial \theta, \tag{1b}$$

$$E_z = -c^{-1} \partial A_z/\partial t. \tag{1c}$$

A_z is itself determined by Ampere's equation,

$$-\nabla_\perp^2 A_z = \frac{4\pi}{c}(J_b + J_p). \tag{2}$$

Here, J_b is the z component of the beam current density, and the plasma current density J_p in (2) is given by σE_z. For a paraxial beam in this regime, transverse currents can be neglected as sources in the field equations.

The equilibrium distribution function f_0 can be defined as any function of the constants of particle motion, the particle energy

$$H = \gamma Mc^2 \equiv (c^2 \underset{\sim}{p}\cdot\underset{\sim}{p} + M^2c^4)^{1/2}, \tag{3}$$

the azimuthal angular momentum

$$P_\theta \equiv r p_\theta, \tag{4}$$

and the axial canonical momentum

$$P_z \equiv p_z + qA_0/c, \tag{5}$$

where $\underset{\sim}{p} = \gamma M \underset{\sim}{v}$ is the particle momentum and A_0 is the equilibrium A_z. Since we consider a non-rotating beam without external fields, we can then take f_0 to be independent of P_θ. To model a paraxial, nearly-monoenergetic beam, we assume that all particles have the same P_z but there is a spread in perpendicular energy

$$H_\perp \equiv H - \gamma_b Mc^2, \tag{6}$$

where

$$\gamma_b Mc^2 \equiv \left(P_z^2 c^2 + M^2 c^4 \right)^{1/2} \tag{7}$$

is the energy associated with P_z. We therefore take f_0 to have the form

$$f_0(H,P_z) = F_0(H_\perp)\ \delta(P_z - P_b). \tag{8}$$

It then follows from the paraxial approximation that v_z is nearly constant for all beam particles and approximately equal to $\beta c \equiv P_z/(\gamma_b M)$. For this distribution function, the equilibrium beam current density is

$$J_{b0}(r) = \frac{2q\beta c}{r} \int_{-\infty}^{\infty} dP_\theta \int_{U(r;P_\theta)}^{\infty} dH_\perp \frac{F_0(H_\perp)}{|v_r(r;H_\perp,P_\theta)|}, \tag{9}$$

where the radial velocity $v_r = p_r/(\gamma M)$ is obtained as a function of r, $H_\perp$, and P_θ from (3)-(5), and the minimum perpendicular energy $U(r;P_\theta)$ in (9) is calculated from the requirement that v_r be real. Since all beam particles in this model have nearly the same axial velocity, it is convenient to use z and $\zeta \equiv \beta ct - z$ as independent variables instead of z and t. Then ζ is a constant of the motion and labels a co-moving slice of the beam, while z describes the time variation in the particle reference frame.

In this paper we are primarily interested in developing an eigenvalue treatment of the hose instability. Since this approach is

possible only if the equilibrium is independent of ζ and z, we require that the beam radius a and the equilibrium beam and plasma densities $J_{b0}(r)$ and $J_{p0}(r)$ are all independent of ζ and z. These quantities are, in fact, slowly varying except near the beam head[9,10], which we do not consider here. In addition, we must ignore the ζ and z dependences of the conductivity $\sigma(r)$, which can result from heating and ionization by the beam. Such σ variations can have a significant effect when the beam-generated conductivity is a large fraction of σ, but this approximation is appropriate for beams propagating in highly preionized channels. We emphasize also that the multi-component model developed in Sec. III is not limited to axially uniform beams. A multi-component "simulation" code, which explicitly retains all ζ and z dependences, has been developed[8] and will be reported in a separate paper.

We formulate the hose eigenvalue problem by decomposing perturbations into independent Fourier modes with azimuthal mode number m=1 and axial wave number k_z. In terms of ζ and z, the perturbed A_z and J_b have the form

$$\begin{bmatrix} A_1(r,\zeta,z) \\ J_1(r,\zeta,z) \end{bmatrix} = \begin{bmatrix} \hat{A}(r) \\ \hat{J}(r) \end{bmatrix} \exp\left(i\theta - i\frac{\omega}{\beta c}\zeta - i\frac{\Omega}{\beta c}z\right), \tag{10}$$

where $\Omega \equiv \omega - k_z\beta c$ is the frequency seen by beam particles, and $\omega/(\beta c)$ can be thought of as a wave number for spatial oscillations in ζ. From Ampere's equation (2), the perturbed A_z satisfies the linearized relation

$$\frac{d}{dr}\frac{1}{r}\frac{d}{dr}r\hat{A} + \frac{4\pi i\omega\sigma(r)}{c^2}\hat{A} = -\frac{4\pi}{c}\hat{J}. \tag{11}$$

The perturbed beam current $\hat{J}$ is obtained from a standard Vlasov analysis,

first integrating the linearized Vlasov equation along unperturbed particle orbits and then integrating over the constants of the motion $H_\perp$ and P_θ. The result[6] is

$$\hat{J}(r) = \frac{2q^2\beta^2 c}{r} \int_{-\infty}^{\infty} dP_\theta \int_U^{\infty} dH_\perp \frac{1}{|v_r|} \frac{dF_0}{dH_\perp} \left[\hat{A}(r) + \frac{i\Omega}{\beta c} \hat{I}(r;H_\perp,P_\theta)\right] , \qquad (12)$$

where

$$\hat{I}(r;H_\perp,P_\theta) = \frac{1}{2} \sum_{\pm} \int_{-\infty}^{z} dz' \hat{A}(r'_{\pm}) \exp\left[i(\theta'_{\pm} - \theta) - i\frac{\Omega}{\beta c}(z'-z)\right]. \qquad (13)$$

In the orbit integral (13), $r'_{\pm}$ and $\theta'_{\pm}$ specify the unperturbed location at $z' < z$ of a particle with $r_{\pm}(z) = r$, $\theta_{\pm}(z) = \theta$, $v_r(z) = \pm |v_r(z)|$, and constants of motion P_θ and $H_\perp$.

B. Particle Orbit Properties

Particle dynamics in the transverse plane is discussed at some length in Appendix A. Here, we summarize the properties which influence the analytic structure of the eigenfunctions and help to motivate the multi-component formalism of Sec. III.

For paraxial beams, v_r is approximated by

$$v_r(r;H_\perp,P_\theta) = \pm \left(\frac{2}{\gamma_b M}\right)^{1/2} \left[H_\perp - U(r;P_\theta)\right]^{1/2} , \qquad (14)$$

where

$$U(r;P_\theta) = \frac{1}{2\gamma_b M} \frac{P_\theta^2}{r^2} - q\beta A_0(r) \qquad (15)$$

is the effective potential that determines the transverse motion of a particle with angular momentum P_θ. Using (14), the perpendicular energy can be expressed as

$$H_\perp \approx \frac{1}{2}\gamma_b M v_r^2 + U(r;P_\theta), \tag{16}$$

which has the form of a particle Hamiltonian in a time-independent axisymmetric potential. Each particle therefore executes periodic oscillations in r while moving azimuthally with an angular velocity $\dot{\theta} = P_\theta/(\gamma_b M r^2)$. Except in the special case where the net current density $J_{n0}(r) \equiv J_{b0}(r) + J_{p0}(r)$ is uniform, the effective potential U is anharmonic. Because of this anharmonicity, particles in general have precessing, unclosed orbits in the transverse plane, and both the radial oscillation frequency

$$\Omega_r = \pi \left[\int_{r_{min}}^{r_{max}} \frac{dr}{|v_r|}\right]^{-1} \tag{17}$$

and the average azimuthal frequency

$$\Omega_\theta \equiv \langle \dot{\theta} \rangle = \frac{\Omega_r P_\theta}{\pi \gamma_b M} \int_{r_{min}}^{r_{max}} \frac{dr}{r^2 |v_r|} \tag{18}$$

depend on $H_\perp$ and P_θ through $v_r(r;H_\perp,P_\theta)$ and the orbit turning points $r_{min}(H_\perp,P_\theta)$ and $r_{max}(H_\perp,P_\theta)$. The orbits close in the r-θ plane only when Ω_r/Ω_θ is rational.

For particles confined near the center of the beam, it is possible to calculate Ω_r and Ω_θ in closed form. In this region, J_{n0} for an unhollowed beam can be approximated by

$$J_{n0}(r) = J_{n0}(0)\ (1 - 2r^2/a_n^2), \tag{19}$$

where a_n is a radial scale length of the net current profile and in typical beams is close to the beam radius a. To lowest order in $r^2/a_n^2 \ll 1$, we then find that

$$\Omega_r(H_\perp, P_\theta) \approx 2\Omega_0\left(1 - \frac{3H_\perp}{4\gamma_b M a_n^2 \Omega_0^2}\right), \tag{20}$$

and

$$\Omega_\theta(H_\perp, P_\theta) \approx \mathrm{sgn}(P_\theta)\Omega_0\left(1 - \frac{3H_\perp - \Omega_0|P_\theta|}{4\gamma_b M a_n^2 \Omega_0^2}\right), \tag{21}$$

where the limiting azimuthal frequency is given by

$$\Omega_0^2 = \frac{2\pi q\beta}{\gamma_b M c} J_{n0}(0). \tag{22}$$

The result that $\Omega_r \to 2\Omega_\theta$ as $P_\theta \to 0$ is physically obvious because an orbit which grazes the axis makes a complete radial oscillation while θ changes by π. Similarly, for particles confined near the axis with $H_\perp \to 0$, the orbits approach closed ellipses with $\Omega_\theta \to \mathrm{sgn}(P_\theta)\Omega_0$ and $\Omega_r \to 2\Omega_0$. We note also from (20) and (21) that both Ω_r and Ω_θ decrease monotonically with $H_\perp$,

$$\left(\frac{\partial\Omega_r}{\partial H_\perp}\right)_{P_\theta} < 0, \qquad \left(\frac{\partial\Omega_\theta}{\partial H_\perp}\right)_{P_\theta} < 0. \tag{23}$$

Numerical evaluation of Ω_r and Ω_θ indicates that (23) holds for all r when $J_{n0}(r)$ is peaked on axis, not just for $r \ll a_n$. However, Ω_r

depends on both $H_\perp$ and P_θ when r/a_n is not small.

It is of interest also to characterize the class of beam particles that have a particular oscillation frequency Ω_θ, since these particles are all resonant with a wave of frequency $\Omega = \Omega_\theta$. Properties of these particles can be calculated in closed form for the case

$$H_\perp \ll q\beta A_0(a_n) \ , \tag{24}$$

which is equivalent to the particles being confined to $r \ll a_n$, where (19) is valid and the effective potential U is nearly harmonic. We show in Appendix A that when (24) holds, the equilibrium current density profile of this class of particles is

$$\delta J_0(r;\Omega_\theta) = \begin{cases} \delta J_0(0;\Omega_\theta)\left[1+\frac{2}{\pi}\sin^{-1}\left(\frac{1}{8}\frac{r^2}{\tilde{R}^2(\Omega_\theta)-r^2}\right)^{1/2}\right], & 0 < r^2 < \frac{8}{9}\tilde{R}^2(\Omega_\theta) \\ 2\delta J_0(0;\Omega_\theta), & \frac{8}{9}\tilde{R}^2(\Omega_\theta) < r^2 < \tilde{R}(\Omega_\theta) \\ 0 \ , & \tilde{R}^2(\Omega_\theta) < r^2, \end{cases} \tag{25}$$

where $\tilde{R}(\Omega_\theta)$, defined as the maximum radius accessible to any particle with the specified value of Ω_θ, is given in the small-orbit limit by

$$\tilde{R}^2(\Omega_\theta) = 3a_n^2\,(1-|\Omega_\theta|/\Omega_0) \tag{26}$$

and occurs for particles with $|P_\theta| = 4\gamma_b M\tilde{R}^2\Omega_0/9$, which have orbits midway between radial ($P_\theta = 0$) and circular ($|P_\theta| = 8\gamma_b M\tilde{R}^2\Omega_0/9$). The profile (25) is shown in Fig. 1, and we note particularly that $\delta J_0(r;\Omega_\theta)$ drops

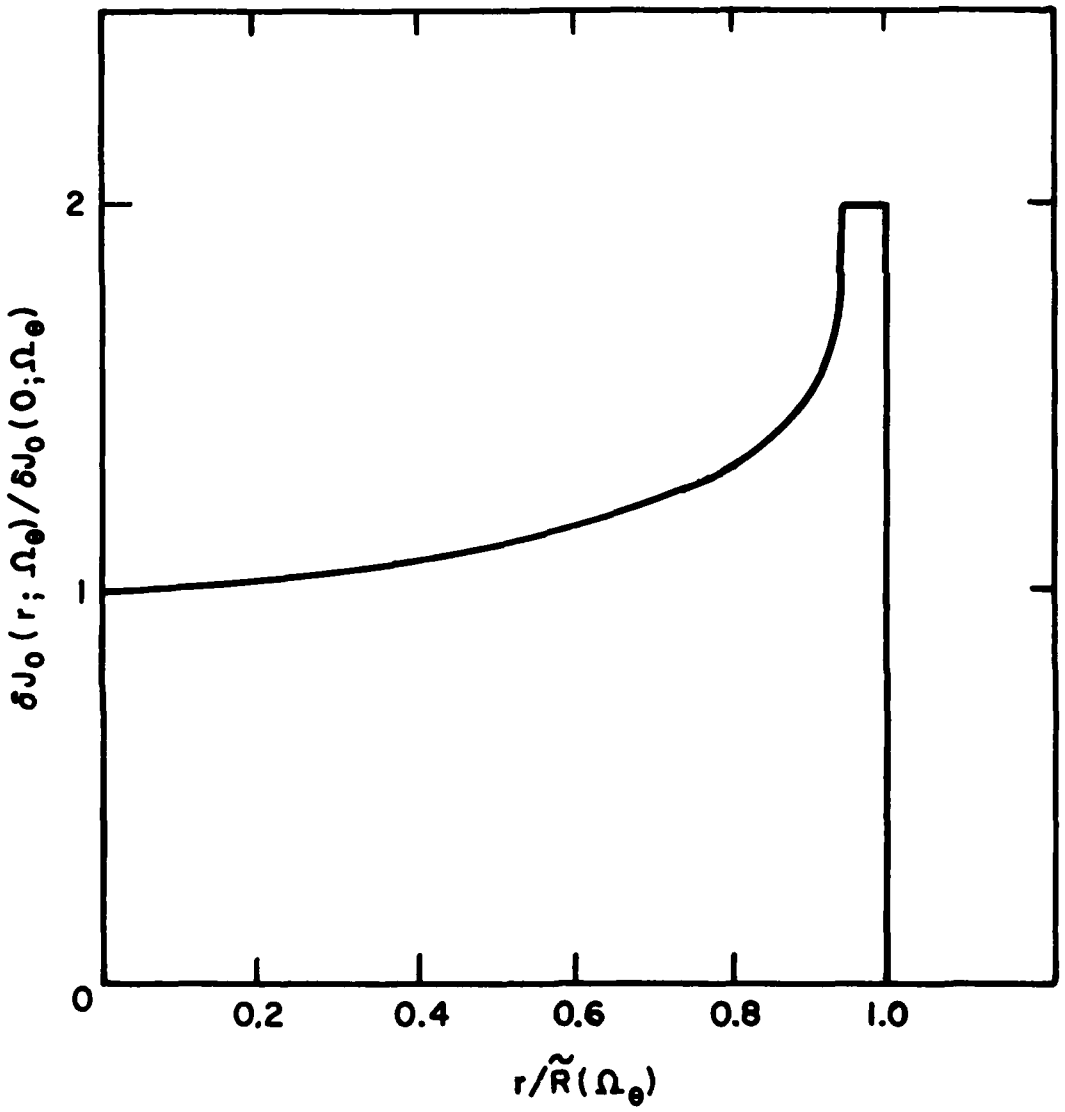

Fig. 1 — Equilibrium current density profile $\delta J_0(r;\Omega_\theta)$ of particles with azimuthal frequency Ω_θ; for the case with $(\Omega_0 - \Omega_\theta) \ll \Omega_0$

discontinuously to zero at $r = \tilde{R}(\Omega_\theta)$.

Numerical calculations for monotonically decreasing $J_{n0}(r)$ profiles show that groups of particles with the same Ω_θ have the qualitative features of (25) and (26) even when r/a_n is not small. All such groups have a hollow current density profile $\delta J_0(r;\Omega_\theta)$ that vanishes discontinuously at some outer radius $\tilde{R}(\Omega_\theta)$. This radius decreases monotonically with Ω_θ because the pinch force becomes weaker than that of a harmonic potential as the radius increases, so that particles whose orbits reach larger radii tend to have a smaller azimuthal frequency Ω_θ. The plot of $\tilde{R}(\Omega_\theta)$ in Fig. 2 for the case of a Bennett profile[11]

$$J_{n0}(r) = J_{n0}(0)\left(1+ r^2/a_n^2\right)^{-2} \tag{27}$$

is typical, and we show in Appendix A that the curve approaches

$$\tilde{R}(\Omega_\theta) = 1.52\, a_n\Omega_0/|\Omega_\theta| \tag{28}$$

for $H_\perp \gg q\beta A_0(a_n)$. Also, the particles with an azimuthal frequency Ω_θ whose orbits pass through $\tilde{R}(\Omega_\theta)$ are found in general to follow orbits that are intermediate between linear and circular. Since $\tilde{R}$ and $|\Omega_\theta|$ normally have a one-to-one functional relationship, we can take Ω_θ to be a function of $\tilde{R}$ and think of $\tilde{R}$ as the independent variable characterizing the class of particles with azimuthal frequency $\Omega_\theta(\tilde{R})$. For later reference, we note the inverses of (26) and (28):

$$\Omega_\theta(\tilde{R}) = \pm\, \Omega_0(1 - \tilde{R}^2/3a_n^2), \qquad \tilde{R} \ll a_n \tag{29}$$

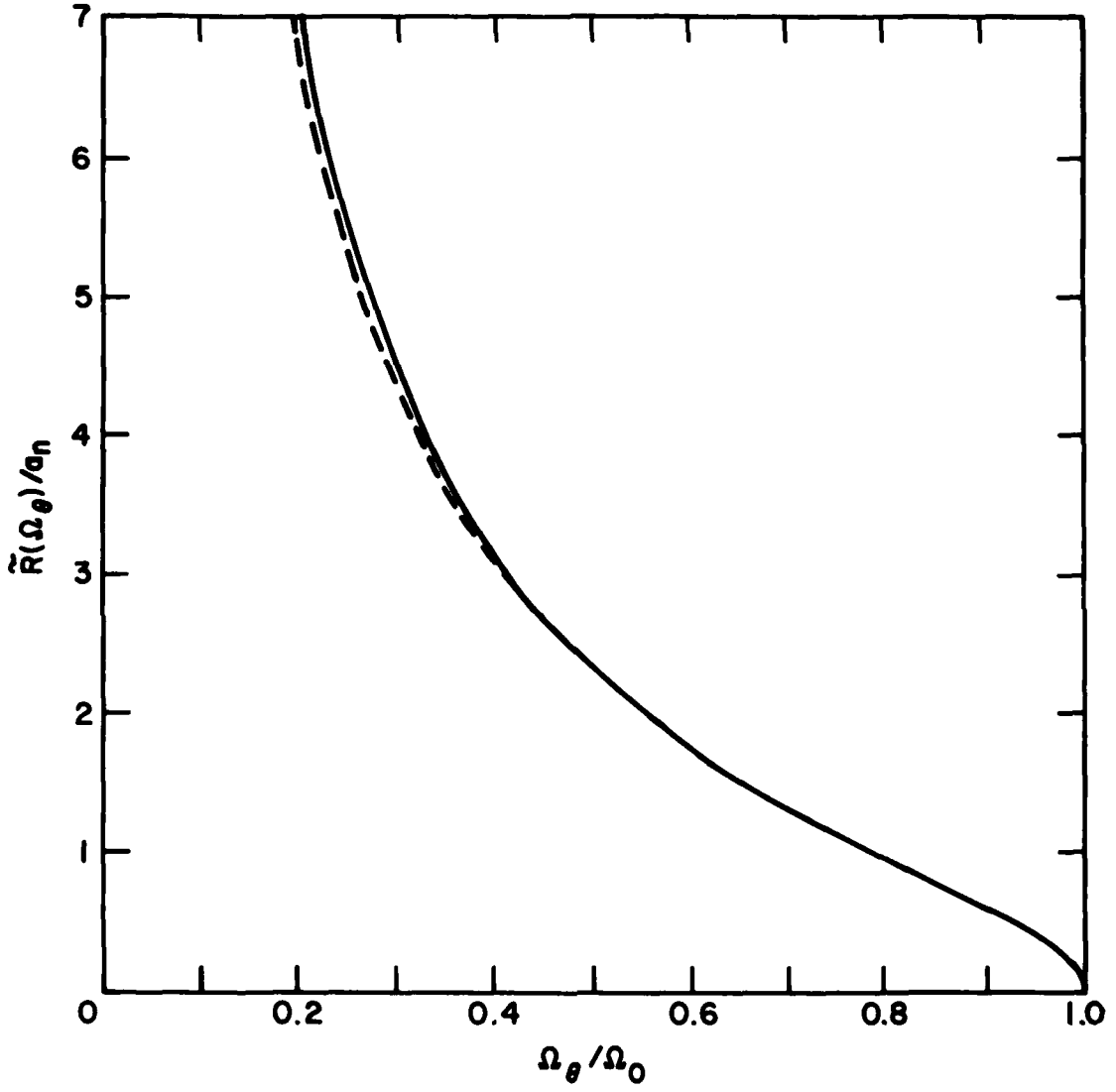

Fig. 2 — Maximum radius $\tilde{R}(\Omega_\theta)$ attained by particles in a Bennett beam with azimuthal frequency Ω_θ, shown by the solid curve. Component radius $R_c(\Omega_\theta)$ is the dashed curve.

$$\Omega_\theta(\tilde{R}) = \pm\ 1.52\ \Omega_0 a_n/\tilde{R}, \qquad \tilde{R} \gg a_n. \tag{30}$$

C. Analytic Properties of $\hat{J}(r)$

The periodicity of the particle orbits makes it possible to rewrite the Vlasov orbit integral $\hat{I}$ in (13) as an integral over r over half of a radial oscillation. The result, derived in Appendix B, is

$$\hat{I}(r;H_\perp,P_\theta) = -i\beta c \int_{r_{min}}^{r_{max}} \frac{dr'\hat{A}(r')}{|v_r(r')|}\left[\frac{\cos\phi(r)\cos\phi(r')}{\tan[\pi(\Omega_\theta-\Omega)/\Omega_r]}\right.$$

$$\left. + \Theta(r-r')\sin\phi(r)\cos\phi(r') + \Theta(r'-r)\sin\phi(r')\cos\phi(r)\right], \tag{31}$$

where ϕ is the phase shift along the orbit,

$$\phi(r;H_\perp,P_\theta) \equiv \int_{r_{min}}^{r} dr' \frac{\dot{\theta}(r';P_\theta)-\Omega}{|v_r(r')|}, \tag{32}$$

and Θ is the step function,

$$\Theta(x) = \begin{cases} 0, & x < 0 \\ 1, & x \geq 0. \end{cases}$$

For clarity, the $H_\perp$ and P_θ dependences of the orbit quantities r_{min}, r_{max}, v_r, Ω_r, Ω_θ, $\dot{\theta}$, and ϕ have been suppressed in (31) and (32). Although (31) could be used in (12) to calculate $\hat{J}(r)$, we are interested here in using the expression to examine the analytic properties of $\hat{J}(r)$.

The integrand of $\hat{I}$ is singular at the zeros of $\tan[\pi(\Omega_\theta-\Omega)/\Omega_r]$, i.e. for real Ω and values of $\Omega_\theta(H_\perp,P_\theta)$ and $\Omega_r(H_\perp,P_\theta)$ that satisfy

$$\Omega = \Omega_\theta + n\Omega_r \tag{33}$$

for any integer n. The principal resonance with n = 0 normally gives the strongest coupling because, according to (32), the variation of ϕ along an orbit is a minimum for this case, and the integrand in (31) is least oscillatory. We therefore consider strongly resonant modes with $\mathrm{Re}\ \Omega \gg \mathrm{Im}\ \Omega$ and $\mathrm{Re}\ \Omega = \Omega_\theta(\tilde{R})$ for some $\tilde{R} \lesssim a_n$. A numerical evaluation of (31) for realistic $\hat{A}$ confirms that the principal resonance is indeed dominant for these modes. Other resonances, mainly n = 1, typically contribute less than 10% to the magnitude of $\hat{I}$, while the nonresonant terms account for less than 2%. We are therefore justified in substituting $\pi(\Omega_\theta - \Omega)/\Omega_r$ for $\tan[\pi(\Omega_\theta - \Omega)/\Omega_r]$ in the first term of (31) and neglecting the nonresonant second and third terms. We also use (23) to change variables from $H_\perp$ to Ω_θ. These manipulations obviously preserve the analytic character of $\hat{I}$ near the principal resonance. The perturbed current (12) can then be written approximately as

$$\hat{J}(r) = 2q^2\beta^2\gamma_b Mc \int_0^{\Omega_\theta(\tilde{R}=r)} d\Omega_\theta \int_{\max(0,P_-)}^{P_+} \frac{dP_\theta}{(P_+ - P_\theta)^{1/2}(P_\theta - P_-)^{1/2}}$$

$$\times \frac{dF_0}{dH_\perp} \left| \frac{\partial H_\perp}{\partial \Omega_\theta} \right|_{P_\theta} \left[\hat{A}(r) + \frac{\Omega}{\Omega_\theta - \Omega} \langle \hat{A} \rangle\right] , \tag{34}$$

where the quantities $P_\pm(r;\Omega_\theta)$, given in Appendix A, are the maximum and minimum $|P_\theta|$ values that formally give $H_\perp \geq U(r;\Omega_\theta)$ and an azimuthal frequency $\pm\,\Omega_\theta$ according to (15) and (21). The Ω_θ integration range in

(34) includes all positive Ω_θ values of particles with orbits passing through r, and

$$\langle \hat{A}(r;\Omega_\theta,P_\theta)\rangle \equiv \pi^{-1}\Omega_r \cos\phi(r) \int_{r_{min}}^{r_{max}} \frac{dr'\hat{A}(r')}{|v_r(r')|}\cos\phi(r') \qquad (35)$$

is an appropriate orbit average of $\hat{A}(r)$ that depends on Ω_θ and P_θ through r_{min}, r_{max}, v_r, and ϕ.

Several analytic properties of $\hat{J}(r)$ are immediately evident from (34):

(i) In the special case $F_0(H_\perp) = \delta(H_\perp - H_b)$, where H_b is a constant, the beam current density profile $J_{b0}(r)$ is flat out to a maximum radius, and the pinch potential is harmonic, provided that J_{p0} is also flat. Then Ω_θ is the same for all particles, and when $\Omega \to \Omega_\theta$, $\hat{J}(r)$ becomes singular as $(\Omega - \Omega_\theta)^{-1}$ at all values of r.

(ii) In the more physical case where $F_0(H_\perp)$ is a non-singular function of $H_\perp$, the beam profile $J_{b0}(r)$ is a smooth, rounded function, and normally $J_{n0}(r)$ is likewise rounded. Then $\hat{J}(r)$ has a singularity at $\tilde{R}(\Omega)$ for real values of $\Omega \leq \Omega_0$,

$$\hat{J}(r) \propto \ln\left[r - \tilde{R}(\Omega)\right] \qquad (36)$$

as $r \to \tilde{R}(\Omega)$.

(iii) As $\Omega \to \Omega_0$, the singular point in $\hat{J}(r)$ moves to $r = 0$. When (34) is rewritten in terms of Ω_θ/Ω, it becomes apparent that $\hat{J}$ depends on r and Ω only through $\bar{r} \equiv r/\tilde{R}(\Omega)$, and that the perturbed field equation (11) reduces to

$$\frac{d}{d\bar{r}}\frac{1}{\bar{r}}\frac{d}{d\bar{r}}\bar{r}\,\hat{A} + \frac{4\pi i\omega\tilde{R}^2\sigma(0)}{c^2}\hat{A} = 0. \tag{37}$$

Thus the destabilizing contribution of the perturbed beam current vanishes in the limit $\Omega \to \Omega_0$, and the hose mode is damped.

If we write (34) in the form

$$\hat{J}(r) = \int_0^{\Omega_\theta(\tilde{R}=r)} d\Omega_\theta \;\; \delta\hat{J}(r;\Omega_\theta) \tag{38}$$

to emphasize the contributions to $\hat{J}$ from groups of particles with a common value of Ω_θ, we see that $\delta\hat{J}(r;\Omega_\theta)$ vanishes at $r = 0$ and goes discontinuously to zero at $r = \tilde{R}(\Omega_\theta)$, the location at which $P_+(r;\Omega_\theta) = P_-(r;\Omega_\theta)$. This discontinuity is responsible for the logarithmic singularity of $\hat{J}(r)$ at $r = \tilde{R}(\Omega)$.

In the next section, we use these properties of $\hat{J}$ to guide the formulation of a macroscopic beam dynamics model.

III. Multi-Component Formalism

A. Beam Dynamics Model

It is evident from the discussion in Sec. IIB that a beam can be thought of as partitioned into groups of particles with the same value of Ω_θ. Each of these groups is localized within $0 \leq r \leq \tilde{R}(\Omega_\theta)$, and all particles in such a group are resonant with a wave of frequency $\Omega = \Omega_\theta$. This radial localization leads to the singularity in $\hat{J}(r)$ at $\tilde{R}(\Omega_\theta)$ found in Sec. IIC. A macroscopic beam dynamics model might therefore represent the resonant structure correctly, provided that it localizes the part of the beam resonant at frequency Ω within radius $\tilde{R}(\Omega)$.

Our approach is to represent the beam slice at axial location ζ as a superposition of components with different radii, each with an equilibrium current density profile of the form

$$\delta J_0(r;R) = \begin{cases} \delta J_0(0;R)G(r/R), & r \leq R \\ 0, & r > R, \end{cases} \tag{39}$$

where $G(0) = 1$. The quantity R is used here to identify the component with radius R, just as either Ω_θ or $\tilde{R}$ was used in Sec. II to identify the group of particles with the same Ω_θ. The beam current $J_{b0}(r)$ is the sum of the component densities,

$$J_{b0}(r) = \int_0^\infty dR\ \delta J_0(r;R). \tag{40}$$

To treat the linearized beam response to an $m = 1$ wave of the form (10), we specify that $\hat{J}(r)$ be the sum of the individual component perturbed densities,

$$\hat{J}(r) = \int_0^\infty dR\ \delta\hat{J}(r;R), \tag{41}$$

and we require that each component respond rigidly to the linearized $\underset{\sim}{J} \times \underset{\sim}{B}$ force averaged over its cross section, so that

$$\delta\hat{J}(r;R) = -\hat{\xi}(R)\frac{\partial}{\partial r}\delta J_0(r;R) \tag{42}$$

where $\hat{\xi}(R)$ is the amplitude of the Fourier-analyzed transverse displacement. From Newton's force law, we find after two integrations by parts that

$$-\Omega^2\hat{\xi}(R) = \frac{\pi q\beta}{\gamma_b M\delta I(R)}\int_0^R dr\ r\left[\delta J_0(r;R)\left(\frac{d\hat{A}}{dr} + \frac{\hat{A}}{r}\right) + \delta\hat{J}(r;R)\frac{dA_0}{dr}\right], \tag{43}$$

where

$$\delta I(R) = 2\pi\int_0^R dr\ r\delta J_0(r;R) \tag{44}$$

is the component current. We note that the second bracketed term in (43) represents the restoring force on the displaced component due to the equilibrium field. Using (42), this term can be written as $-\Omega_c^2(R)\hat{\xi}(R)$, where

$$\Omega_c^2(R) = \frac{\pi q\beta}{\gamma_b M\delta I(R)}\int_0^R dr\ r\frac{dA_0}{dr}\frac{\partial}{\partial r}\delta J_0(r;R) \tag{45}$$

is the natural oscillation frequency of the component with radius R in the equilibrium field. Equation (43) can then be rewritten

$$\hat{\xi}(R) = \frac{\pi q\beta}{\gamma_b M\delta I(R)}\frac{1}{\Omega_c^2(R) - \Omega^2}\int_0^R dr\ r\hat{A}(r)\frac{\partial}{\partial r}\delta J_0(r;R), \tag{46}$$

which explicitly displays the resonance at $\Omega_c^2(R) = \Omega^2$. It is evident that $\Omega_c(R)$ plays a role similar to that of the individual particle frequency $\Omega_\theta(\tilde{R})$, although we should recall that the component executes linearly polarized simple harmonic oscillations with no azimuthal motion, whereas individual particles follow complicated precessing orbits in the transverse plane.

The Vlasov analysis of Sec. II shows that the group of particles with a given value of Ω_θ does not in fact respond rigidly to a transverse force. Nonetheless, we can choose the component shape $G(r/R)$ so that the perturbed current density $\delta\hat{J}(r;R)$ of a component reproduces the properties of the Vlasov perturbed current contribution $\delta\hat{J}(r;\Omega_\theta)$. As noted in Sec. IIC, $\delta\hat{J}(r;R)$ should be a continuous function on $0 \leq r < R$, that vanishes smoothly at $r = 0$ and drops discontinuously to zero at $r = R$. We choose the convenient mathematical form

$$\delta J_0(r;R) = \delta J_0(0;R)\ (1 - r^\ell/R^\ell)\ \Theta(R - r), \tag{47}$$

which satisfies these requirements and yet allows the component profile to be varied from a triangular shape to a step function by varying ℓ from unity to infinity.

With this component shape, (40) can be solved for the coefficient of δJ_0,

$$\delta J_0(0;R) = \frac{1}{\ell}\left[r\,\frac{d^2 J_{b0}}{dr^2} - (\ell-1)\,\frac{dJ_{b0}}{dr}\right]_{r=R}, \tag{48}$$

and the component current (44) is

$$\delta I(R) = \frac{\ell}{\ell+2}\,\pi R^2 \delta J_0(0;R)\ . \tag{49}$$

Combining these expressions with (41), (42), and (46) then gives

$$\hat{J}(r) = \frac{(\ell+2)q\beta}{\gamma_b M}\ r^{\ell-1}\int_r^\infty \frac{dR}{R^{2\ell+2}}\left[r\,\frac{d^2 J_{b0}}{dr^2} - (\ell-1)\,\frac{dJ_{b0}}{dr}\right]_{r=R}$$

$$\times\ \frac{1}{\Omega_c^2(R) - \Omega^2}\int_0^R dr' r'^{\ell}\,\hat{A}(r'), \tag{50}$$

where, from (45),

$$\Omega_c^2(R) = \frac{4\pi q\beta}{\gamma_b Mc}\ \frac{\ell+2}{\ell}\ \frac{1}{R^2}\int_0^R dr\ r\left(1 - \frac{r^\ell}{R^\ell}\right)(J_{b0} + J_{p0}). \tag{51}$$

Comparing (51) with (22), we see that

$$\Omega_c^2(0) = \Omega_0^2\ , \tag{52}$$

independent of ℓ. For real Ω values less than the maximum Ω_c, the resonant denominator in (50) can be represented near the singularity as

$$[R - R_c(\Omega)]\left(\frac{d\Omega_c^2}{dR}\right)_{R=R_c(\Omega)},$$

where $R_c(\Omega)$ is the radius of the component with $\Omega_c = \Omega$ and may be thought of as the inverse function of (51). This pole in the integrand of (50) leads to a logarithmic singularity in $\hat{J}(r)$ at $r = R_c(\Omega)$, in agreement with the Vlasov result.

To choose an appropriate value for the index ℓ in the component profile (47), we examine the $\hat{J}(r)$ expression (50) as $\Omega \to \Omega_0$. Since

$\Omega_0 - \Omega_c(R)$ varies like R^2 for small R, the resonant denominator in (50) can be approximated for $\Omega \to \Omega_0$ by

$$\frac{1}{2}\left[P^2 - P_c^2(\Omega)\right]\left(\frac{d^2\Omega_c^2}{dR^2}\right)_{R=0}.$$

We can then write (50) in terms of $\bar{r} \equiv r/R_c(\Omega)$ and $\bar{R} \equiv R/R_c(\Omega)$:

$$\hat{J}(\bar{r}) \approx -\frac{\ell(\ell+4)q\beta}{\gamma_b M}\frac{a_n^2}{\Omega_0^2}\frac{\bar{r}^{\ell-1}}{R_c^3(\Omega)}\int_{\bar{r}}^{\infty}\frac{d\bar{R}}{\bar{R}^{2\ell+2}}\frac{\delta J_0[0;R_c(\Omega)\bar{R}]}{\bar{R}^2-1}\int_0^{\bar{R}}d\bar{r}'\bar{r}'^{\ell}\hat{A}(\bar{r}'). \qquad (53)$$

We note from (48) that for $\ell = 2$, $\delta J_0(0;R) \propto R^3$ for small R, whereas for any other value of ℓ, $\delta J_0(0;R) \propto R$. Consequently, as $R_c(\Omega) \to 0$, $\hat{J}(\bar{r})$ is independent of $R_c(\Omega)$ when $\ell = 2$ and becomes negligible compared with

$$\frac{d}{dr}\frac{1}{r}\frac{d}{dr}r\hat{A} = \frac{1}{R_c^2(\Omega)}\frac{d}{d\bar{r}}\frac{1}{\bar{r}}\frac{d}{d\bar{r}}\bar{r}\hat{A}, \qquad (54)$$

so that the $\hat{A}$ equation (11) takes the form of the Vlasov result (37). For other values of ℓ, $\hat{J} \propto R_c^{-2}(\Omega)$ in the same limit. We thus conclude that $\ell = 2$ is the only physically acceptable choice.

With $\ell = 2$, the multi-component expression (53) for $\delta\hat{J}$ also shows remarkable agreement with the Vlasov result in other respects. The multi-component resonance location $R_c(\Omega)$ is compared with the Vlasov resonance location $\tilde{R}(\Omega)$ in Fig. 2. The two quantities agree to within 5% everywhere and to much greater accuracy for the large fraction of beam particles with $r_{max}/a_n \lesssim 2$. In the limit $\Omega \to \Omega_0$, (51) gives

$$\Omega_c(R) = \Omega_0(1 - R^2/3a_n^2) \qquad (55)$$

for $\ell = 2$, in exact agreement with the Vlasov expression (29) for $\Omega_\theta(\tilde{R})$. In the opposite limit, $\Omega \to 0$, the multi-component expression is

$$\Omega_c(R) = 2^{1/2}\, \Omega_0 a_n / R, \tag{56}$$

the coefficient here agreeing with the Vlasov result (30) to within 5%. In addition, a numerical evaluation of $\hat{J}(r)$ for the two models, using realistic J_{b0} and $\hat{A}$ profiles in (12) and (50), shows agreement within 7% in the perturbed current magnitude. This suggests that the multi-component model accurately represents the strength of resonances, as well as their location and analytic form.

B. Calculation of Eigenmodes

We formulate a hose eigenvalue equation by substituting the multi-component $\hat{J}$ expression (50) with $\ell = 2$ into the $m = 1$ field equation (11). The result is

$$\frac{d}{dr}\frac{1}{r}\frac{d}{dr} r\hat{A} + \frac{4\pi i\omega\sigma}{c^2}\hat{A}$$

$$= -\frac{16\pi q\beta}{\gamma_b Mc}\, r \int_r^\infty \frac{dR}{R^4}\left(\frac{d}{dr}\frac{1}{r}\frac{dJ_{b0}}{dr}\right)_{r=R} \frac{1}{\Omega_c^2(R) - \Omega^2} \int_0^R dr' r'^2\, \hat{A}(r'), \tag{57}$$

where, from (51),

$$\Omega_c^2(R) = \frac{8\pi q\beta}{\gamma_b Mc}\, \frac{1}{R^2} \int_0^R dr\, r\left(1 - \frac{r^2}{R^2}\right)\left(J_{b0} - J_{p0}\right). \tag{58}$$

Boundary conditions are obtained from the requirement that

$$\hat{A}(0) = 0 \tag{59}$$

for an m = 1 mode and from the far-field solution of (57)

$$\hat{A} \propto \frac{1}{r} . \tag{60}$$

This eigenvalue problem can be solved for either $\omega(\Omega)$ or $\Omega(\omega)$. It is apparent from (10) that a wave with real Ω and Im $\omega > 0$ has constant amplitude at a given beam slice but grows spatially back from the beam head (i.e. with increasing ζ). Similarly, a mode with real ω grows with increasing z if Im $\Omega > 0$. We concentrate here on modes with real Ω because these modes show the effects of localized resonances most clearly.

To solve the dispersion equation numerically we first rewrite (57) as a homogeneous, fourth-order ordinary differential equation,

$$\frac{d}{dr}\frac{1}{r}\frac{d}{dr}\frac{1}{r}\frac{d}{dr}\left(r\frac{d\Gamma}{dr} + 2\Gamma\right) + \frac{4\pi i\omega}{c^2}\frac{d}{dr}\left[\frac{\sigma}{r^2}\left(r\frac{d\Gamma}{dr} + 2\Gamma\right)\right]$$

$$- \frac{16\pi q\beta}{\gamma_b Mc}\frac{1}{r^2}\left(\frac{d}{dr}\frac{1}{r}\frac{dJ_{b0}}{dr}\right)\frac{\Gamma}{\Omega_c^2(r) - \Omega^2} = 0, \tag{61}$$

where

$$\Gamma(r) \equiv \frac{1}{r^2}\int_0^r dr' r'^2 \hat{A}(r'). \tag{62}$$

This definition of Γ and the two constraints on $\hat{A}$, (59) and (60), give an appropriate set of boundary conditions:

$$\begin{aligned} \Gamma(0) &= 0 \\ \Gamma'(0) &= 0 \\ \lim_{r \to \infty} \Gamma'(r) &= 0 \\ \lim_{r \to \infty} \Gamma''(r) &= 0. \end{aligned} \tag{63}$$

We reduce (61) to a homogeneous matrix equation by representing the derivatives by finite differences on a nonlinear mesh, with grid points clustered near the axis and any resonances. For real Ω, appropriate jump conditions at resonance points are provided by local power series solutions of (61). Eigenfrequencies are calculated by specifying ω or Ω and iteratively adjusting the other frequency until the matrix determinant vanishes. The corresponding eigenfunctions are calculated by the method of inverse interation.[12]

C. Equilibrium Specification for Beams with Return Current

Although the dispersion equation (61) can be solved for any choice of $J_{p0}(r)$ and $J_{b0}(r)$ that give a non-negative Ω_R^2, an arbitrarily chosen J_{b0} may correspond to a physically unlikely distribution function. Here, instead, we specify a Maxwell-Boltzmann distribution function,

$$F_0(H_\perp) = \frac{J_{b0}(0)}{2\pi\gamma_b M q \beta c H_b} \exp\left(-\frac{H_\perp}{H_b}\right), \tag{64}$$

and also specify the conductivity profile $\sigma(r)$ and the effective net current fraction, defined as

$$f_e \equiv \frac{2\pi c}{I_b^2} \int_0^\infty dr\, r^2 \left| J_{b0} \frac{dA_0}{dr} \right|. \tag{65}$$

The equilibrium electric field $E_{z0} = -\beta\partial A_0/\partial\zeta$ is taken to be independent of r, which is a good approximation for $r \lesssim a$. The equilibrium beam current expression (9) can be evaluated analytically in this case and gives

$$J_{b0}(r) = J_{b0}(0)\ \exp(q\beta A_0/H_b), \tag{66}$$

and substituting this expression into (65) gives

$$f_e = \frac{2c}{q\beta I_b}\ H_b, \tag{67}$$

an expression of the Bennett pinch condition[11]. For a given I_b, the effective net current f_e depends only on the perpendicular temperature H_b and can be specified independently of J_{p0}. The equilibrium potential A_0 is calculated by numerically integrating Ampere's equation (2) in the form

$$\frac{1}{r}\frac{d}{dr}\ r\ \frac{dA_0}{dr} = -\frac{4\pi}{c}\ [J_{b0}(r) - \sigma(r)E_{z0}], \tag{68}$$

where J_{b0} is given by (66) and (67) as

$$J_{b0}(r) = J_{b0}(0)\ \exp\left[\ \frac{2c}{f_e I_b}\ A_0(r)\right], \tag{69}$$

and E_{z0} is determined iteratively by requiring that

$$I_b = 2\pi \int_0^\infty dr\ r\ J_{b0}(r). \tag{70}$$

This procedure yields a Bennett current profile[11]

$$J_{b0}(r) = J_{b0}(0)\left(1 + \frac{r^2}{a^2}\right)^{-2} \tag{71}$$

with a beam radius

$$a = \left(\frac{I_b}{\pi J_{b0}(0)}\right)^{1/2} \tag{72}$$

either when $E_{z0} = 0$ or when σ has the same radial dependence as (71).

D. Comment on the "Energy-Group" Model

In Ref. 6 we used a multi-component model with a simple component current density

$$\delta J_0(r;R) = \delta J_0(0;R)\,\Theta(R-r), \tag{73}$$

which corresponds to (47) with $\ell \to \infty$. These components were referred to as energy groups because each one represented the group of particles with some particular value of perpendicular energy $H_\perp$. Unfortunately, the present analysis shows that this component shape is incorrect. The result of using (73) in the multi-component $\hat{J}$ expression (50) is

$$\hat{J}(r) = \frac{q\beta}{\gamma_b M}\,\frac{\hat{A}(r)}{\Omega_c^2(r) - \Omega^2}\,\frac{1}{r}\frac{dJ_{b0}}{dr}\,. \tag{74}$$

Equation (74) gives a pole in $\hat{J}(r)$ at $r = R_c(\Omega)$, rather than the logarithmic singularity found by the Vlasov analysis of Sec. II. Substituting (74) into (11) leads to a second-order dispersion relation

$$\frac{d}{dr}\frac{1}{r}\frac{d}{dr}\,r\hat{A}(r) + \frac{4\pi i\omega\sigma(r)}{c^2}\,\hat{A}(r) = \frac{4\pi q\beta}{\gamma_b Mc}\,\frac{\hat{A}(r)}{\Omega_c^2(r) - \Omega^2}\,\frac{1}{r}\,\frac{dJ_{b0}}{dr}\,, \tag{75}$$

which duplicates (45) in Ref. 6. In the limit $\Omega \to \Omega_0$, (75) can be put in the form

$$\frac{d}{d\bar{r}}\frac{1}{\bar{r}}\frac{d}{d\bar{r}}\,\bar{r}\hat{A}(\bar{r}) + \frac{4\pi i\omega R_c^2(\Omega)\sigma(0)}{c^2}\,\hat{A}(\bar{r}) = \frac{4}{1-\bar{r}^2}\,\frac{J_{b0}(0)}{J_{n0}(0)}\,\frac{a_n^2}{a^2}\,, \tag{76}$$

where $\bar{r} \equiv r/R_c(\Omega)$, a_n is the net current scale radius defined by (15), and a is the analogous beam current radius. According to (76), $\omega R_c^2(\Omega)$ remains constant as $\Omega \to \Omega_0$. Since $R_c^{-2}(\Omega) \propto (\Omega_0 - \Omega)^{-1}$, this model predicts a pole in ω for $\Omega = \Omega_0$ and an infinite growth rate Im ω as $\Omega \to \Omega_0$ from below. The correct result is that the wave is damped in this limit.

This sensitivity of the solution to the component shape motivated the Vlasov analysis of Sec. II and the more careful choice of component shape in Sec. IIIA.

IV. Results

We have numerically solved the multi-component hose eigenvalue problem discussed in Sec. III for real Ω and various choices of effective net current fraction f_e, beam current profile $J_{b0}(r)$, and conductivity profile $\sigma(r)$. The results are discussed in this section.

A. Eigenfunctions

(i) Resonant eigenfunctions. In the usual case where the net current density profile $J_{n0}(r)$ is bell-shaped and peaked on the axis, $\Omega_c(R)$ also peaks on-axis and modes with real $\Omega < \Omega_0$ are resonant at $r = R_c(\Omega)$. A typical hose eigenfunction for such a mode is shown in Fig. 3. As expected, there is a logarithmic singularity in the perturbed current at $r = R_c(\Omega)$, and we note that the perturbation is essentially confined within $0 < r < R_c$. Varying Ω or f_e changes R_c and therefore the width of these resonant eigenfunctions, but their shape is hardly affected: If $\hat{A}$ and $\hat{J}$ are plotted as functions of r/R_c, they are nearly independent of Ω and f_e so long as Ω_c is monotone decreasing with R.

The resonant structure of these eigenmodes, properly regarded as internal disruptions localized within resonances, is ignored in the earlier rigid-beam[1,2] and spread-mass[5] hose dynamics models, where the perturbed current $\hat{J}(r)$ is taken to be simply a rigid displacement of the entire beam.

(ii) Doubly resonant eigenfunctions. When the radial profile of $J_{p0}(r)$ is narrower than that of $J_{b0}(r)$ and f_e is large enough, the net current density $J_{n0}(r)$ can peak away from the axis. In this case, $\Omega_c(R)$ also peaks off-axis, and a mode with real $\Omega < \max(\Omega_c)$ is resonant at two different radii that satisfy $\Omega_c(R) = \Omega$. We then find

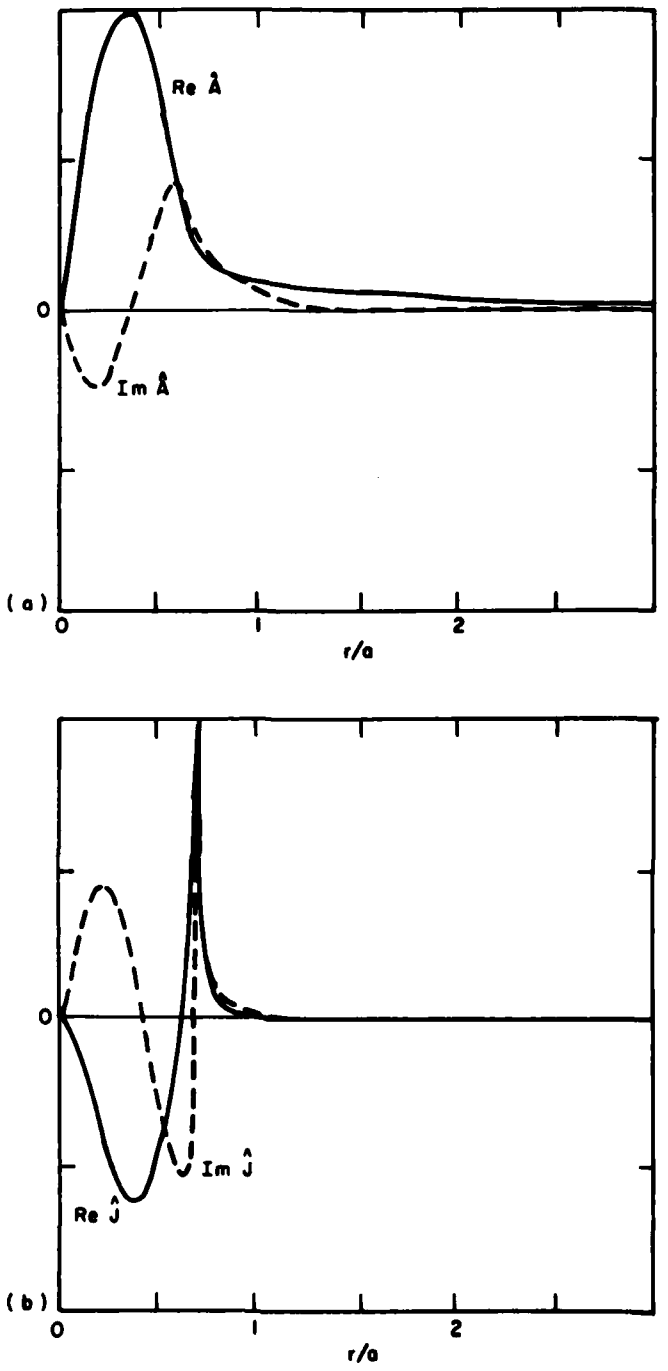

Fig. 3 — (a) Real and imaginary parts of $\hat{A}(r)$ for a typical hose eigenfunction with Ω real. In this case, J_{b0} and σ have Bennett profiles with radius a, and we have $\Omega/\Omega_0 = 0.8$ and $R_c(\Omega)/a \approx 0.7$. (b) Real and imaginary parts of $\hat{J}(r)$ for the same mode as (a).

that the perturbation is largely confined between the two resonant radii, as shown in Fig. 4.

(iii) Non-resonant eigenfunctions. Modes with $\Omega > \Omega_0$ or with significant Im Ω are not resonant. We find then that the form of the eigenfunctions is closer to that of a simple displacement of the beam, where

$$\hat{J}(r) \propto dJ_{b0}/dr.$$

(iv) Higher radial eigenmodes. For any value of Ω, there is an infinite sequence of eigenmodes corresponding to increasing radial quantum number.[3] For beams with a Bennett profile and no return current, we invariably have found these modes to be strongly damped. Earlier work indicates that some of these modes may be unstable for flat beam profiles[3] and for cases with a large return current fraction[6,13], but we have not examined these cases.

B. Dispersion Characteristics

The eigenvalue equation (57) is conveniently put into dimensionless form by introducing the scaled quantities r/a, $\omega\tau_d$, and Ω/Ω_{00}, where

$$\tau_d \equiv \frac{1}{2}\frac{\pi\sigma(0)a^2}{\beta c^2} \tag{77}$$

is the decay time for dipole fields[5,6] and

$$\Omega_{00}^2 \equiv \frac{2\pi q\beta J_{b0}(0)}{\gamma_b Mc} \tag{78}$$

is the value Ω_0^2 would take in the absence of return current, given in terms of the beam plasma frequency $\omega_p(r)$ by $\frac{1}{2}\beta^2\omega_p^2(0)$. The resulting

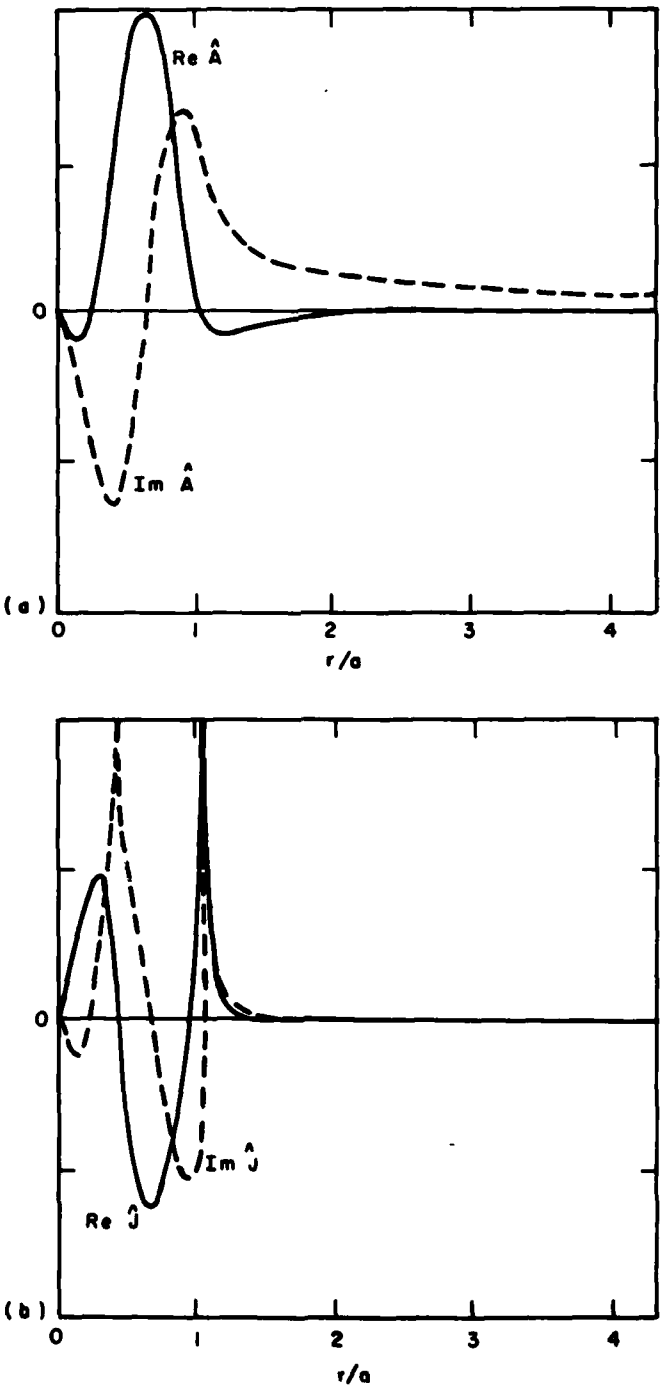

Fig. 4 — (a) Real and imaginary parts of $\hat{A}(r)$ for a hose eigenfunction with two resonance points and $\Omega/\Omega_0 = 1.3$. (b) Real and imaginary parts of $\hat{J}(r)$ for the same mode as (a).

eigenvalue problem is independent of a, β, γ_b, $\sigma(0)$, and J_{b0}. The dispersion relation can therefore be quite generally expressed as a functional relationship between $\omega\tau_d$ and Ω/Ω_{00}, depending only on the scaled quantities $\sigma(r)/\sigma(0)$, $J_{b0}(r)/J_{b0}(0)$, and $\Omega_c(r)/\Omega_{00}$. We present our dispersion results in this form.

(i) No return current. The hose growth rate $\mathrm{Im}(\omega\tau_d)$ and the frequency $\mathrm{Re}(\omega\tau_d)$ are plotted as the solid curves in Fig. 5 for the case where $J_{b0}(r)$ and $\sigma(r)$ have Bennett profiles of equal width. We note that instability occurs only over the range $0 < \Omega/\Omega_{00} < 0.78$, with the maximum growth rate $\omega\tau_d = 0.65$ occurring at $\Omega/\Omega_{00} = 0.57$. We note that $\omega = 0$ when $\Omega = 0$, so that a beam displaced rigidly from the conductivity channel axis is neutrally stable, reflecting the fact that there is no net force on the beam in the absence of plasma current. For $0 < \Omega/\Omega_0 < 1$ the growth rate is determined by competition between the resonant wave-particle coupling and phase mixing due to the betatron frequency spread. Even though resonance effects are stronger as $\Omega \to \Omega_0$, the number of resonant particles, given approximately by (49), decreases as $R_c \to 0$, and for $\Omega/\Omega_{00} > 0.78$ the damping dominates. A dispersion relation of this type leads to convective instability in the beam frame[5], i.e. a perturbation introduced at some point along the beam will grow as it propagates back in ζ but will eventually decay at any given value of ζ.

This case has previously been studied using the energy-group model[6] and the spread-mass model[5]. An exact solution of the energy-group dispersion equation (75) gives a growth rate $\mathrm{Im}\,\omega(\Omega)$ that agrees well with our present result for $\Omega/\Omega_{00} \lesssim 0.6$, but continues to increase to a pole at $\Omega/\Omega_{00} = 1$, for reasons discussed in Sec. IIID. However, the

variational method used in Ref. 6 to approximately solve (75) reduces the resonance strength and leads to the dashed curves in Fig. 5, which agree well with the multi-component result. In the spread-mass model, each slice of the beam is subdivided into rigid components which have density profiles identical to the beam itself. The perturbed current is thus constrained to be a rigid displacement of the slice as a whole, and there is no correlation between the radial extent of a component and its resonant frequency. The components carry equal fractions of the beam current, but a realistic spread in their oscillation frequencies is introduced by assigning the components different masses. For a beam with a Bennett density profile, the resulting dispersion relation is identical to the variational approximation of the energy-group expression, plotted in Fig. 5 as dashed curves, and it agrees remarkably well with our multi-component result over the entire unstable range. The reason for this good agreement is that, for a Bennett profile with no return current, the unstable frequencies have resonant radii $R_c(\Omega)/a > 1$, so that the components which interact most strongly with the wave are nearly as broad as the spread-mass components. Consequently, the resonant components in the two models respond similarly. For waves with $\Omega/\Omega_{00} \sim 1$ and $\tilde{R}/a_n \ll 1$, which have stronger resonant effects, the two growth spectra become quite different, even though the modes are damped and therefore physically unimportant.

The growth spectra for both the spread-mass and multi-component models are sensitive to the equilibrium beam density profile J_{b0}, and the two models do not agree as well for other beam profiles as they do for the Bennett profile. For a Gaussian profile

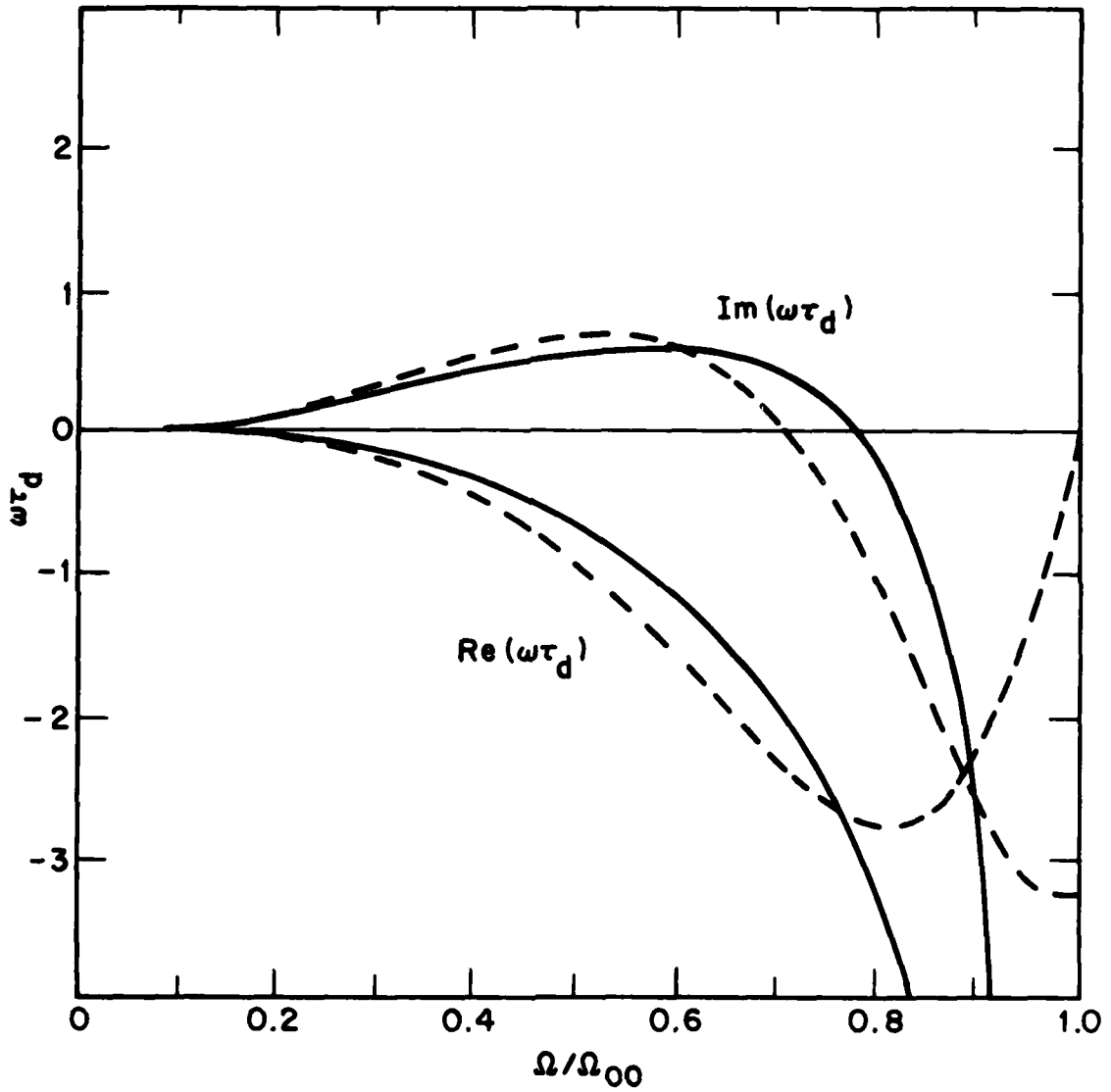

Fig. 5 — Real eigenfrequencies Re ω and growth rates Im ω for the hose modes with Ω real, calculated for a Bennett beam. The solid curves are obtained using the multi-component model; dashed curves come from the spread-mass model or the variational approximation to the energy-group model.

$$J_{b0}(r) = J_{b0}(0)\ \exp(-r^2/a^2)\ , \tag{79}$$

the spread-mass formalism can be applied only if the conductivity has the broadened form

$$\sigma(r) = \sigma(0)\ \frac{r^2}{a^2}\ \frac{\exp(-r^2/a^2)}{1 - \exp(-r^2/a^2)}\ . \tag{80}$$

The growth spectrum from the multi-component treatment is shown for this case as the solid curve in Fig. 6. The curve is more sharply peaked near the maximum growth rate than the Bennett result in Fig. 5 because there are fewer particles with Ω_c/Ω_{00} near 0 and 1. The corresponding spread-mass result, plotted in Fig. 6 as a dashed curve, is broader than the multi-component curve and is shifted to larger Ω values since the mass distribution in this case has more low-mass particles. The dotted curve in Fig. 6 is the growth spectrum calculated from the multi-component dispersion equation using (79) for J_{b0} and a similar Gaussian profile for σ. This is a more realistic conductivity profile than (80) for a Gaussian beam and gives a substantially higher maximum growth rate because the wave-driven dipole return current is confined nearer the axis. This sensitivity to the width of the conductivity channel is a general feature of the hose instability and is discussed subsequently.

(ii) Effect of return current. The presence of equilibrium plasma current worsens the instability by magnetically repelling the displaced beam, and this repulsion is increased when a narrow σ channel confines J_{p0} and the perturbed plasma current near the axis. Figure 7 shows the effect on the hose growth spectrum of a nonzero return current fraction $f_r \equiv 1-f_e$ when J_{b0} and σ both have Bennett profiles with the same

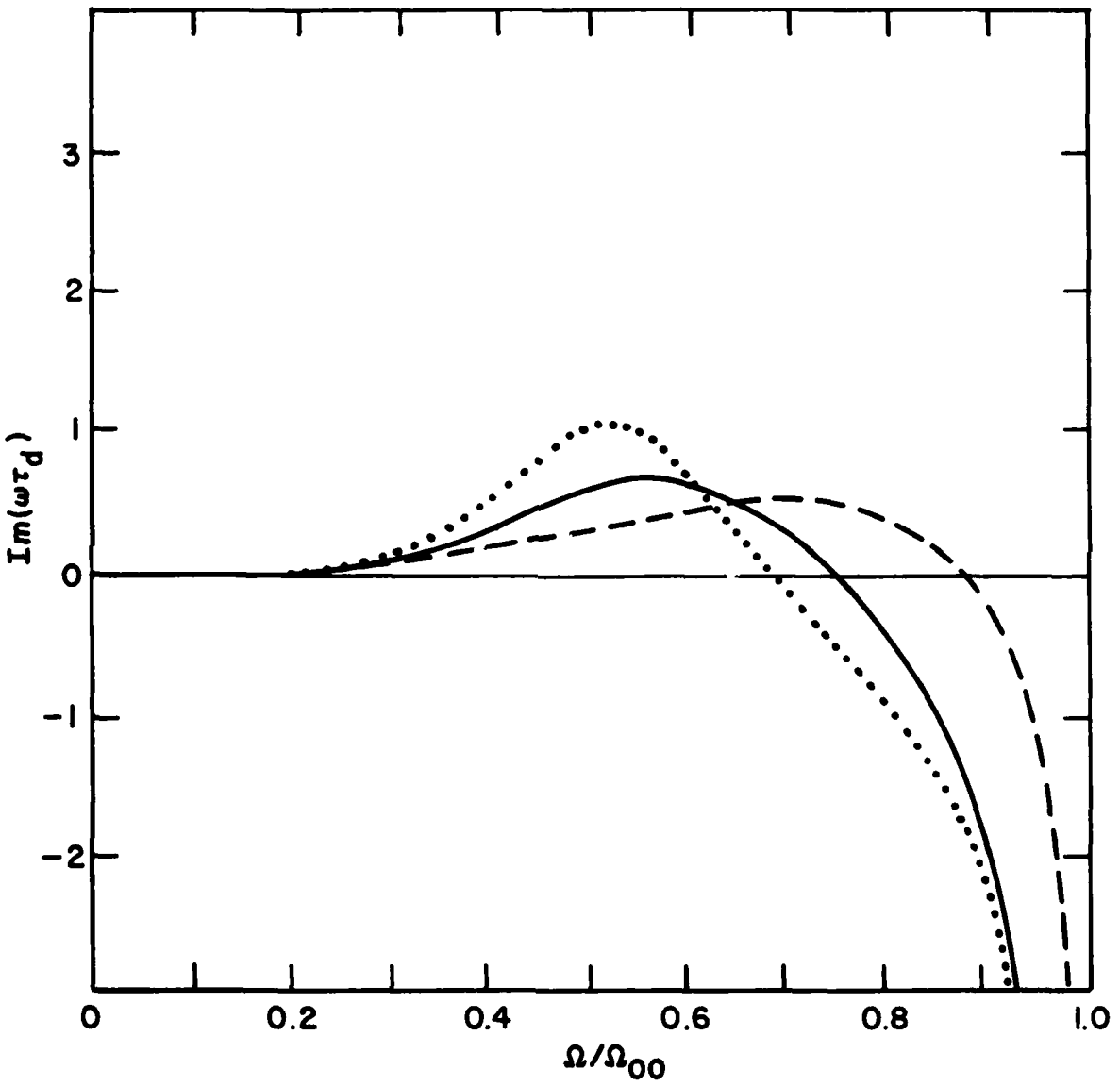

Fig. 6 — Hose growth rates for a beam with a Gaussian current density profile. The multi-component model gives the dotted curve for a Gaussian conductivity profile and the solid curve for a broadened σ profile. The dashed curve comes from the spread-mass model, which required the broadened σ profile.

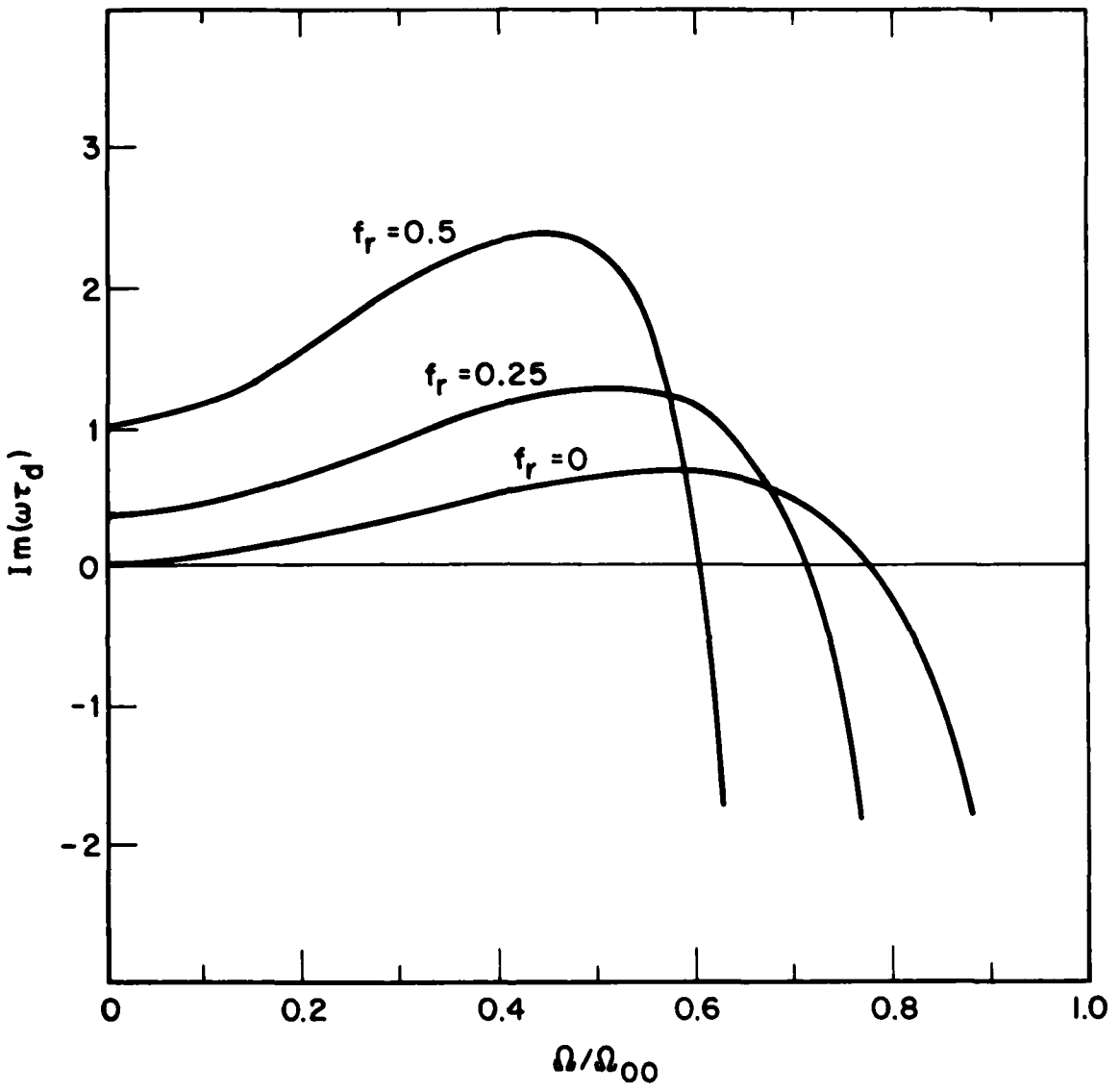

Fig. 7 — Hose growth rates for beams with different values of f_r

radius. The return current is seen to be the dominant destabilizing factor when $f_r \gtrsim 0.3$, and for these f_r values the maximum growth rate increases approximately proportionally to f_r, as expected for pure magnetic repulsion.[6] In this case, Im $\omega > 0$ even for $\Omega = 0$, so that a beam that is rigidly displaced from the conductivity channel axis is pushed further away. This is an absolute instability in the beam frame.

(iii) Narrow conductivity channel. A narrow conductivity channel can also substantially increase hose growth by preventing the perturbed plasma current from following the beam distortion, even when there is no equilibrium plasma current. The growth spectra in Fig. 8 are calculated for beams with $J_{p0} = 0$ and a Bennett profile of $\sigma(r)$ with a radius different from that of the beam. We see a dramatic increase in the maximum growth rate when the ratio α of the conductivity radius to the J_{b0} radius is less than unity. Broadening the conductivity channel, so that $\alpha > 1$, has a stabilizing effect on hose modes, but the effect is less pronounced than for narrow channels because $\hat{A}$ is still confined within $R_c(\Omega)$ and largely determines the radial profile of the plasma current when σ is broad and $J_{p0} = 0$.

(iv) Return current and narrow conductivity channel. Figure 9 shows the growth spectra for a case with equilibrium return current $f_r = 0.25$, and several α values. As expected, the presence of return current and a narrow conductivity channel act together to increase the growth rate even more rapidly.

C. Concluding Remarks

We have developed a tractable model of the resistive hose instability which retains many features of a full Vlasov treatment, and

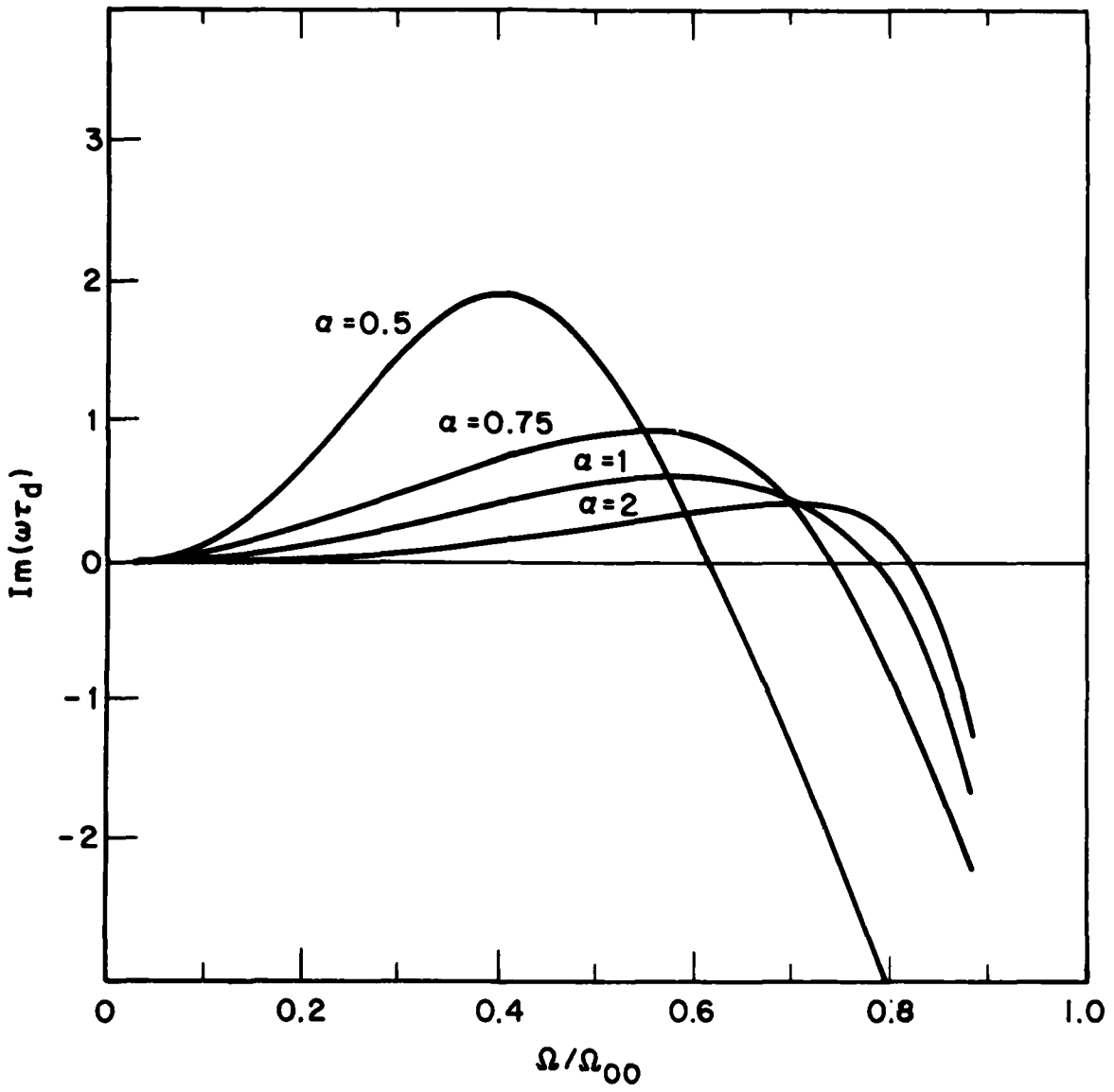

Fig. 8 — Hose growth rates for $f_r = 0$ and different values of α

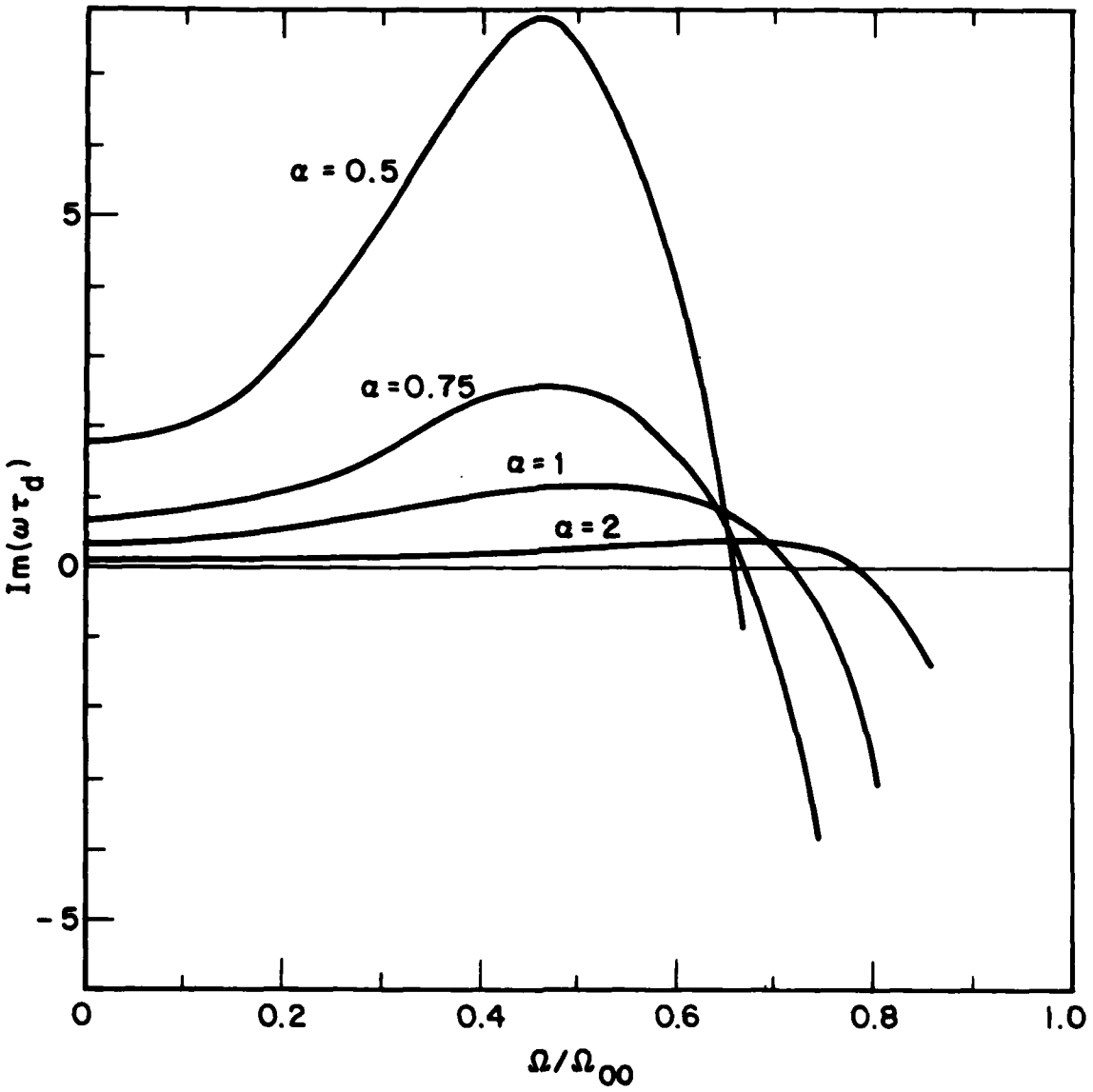

Fig. 9 — Hose growth rates for $f_r = 0.25$ and different values of α

we have used the model to examine the dispersion relation and eigenfunctions in a variety of cases. The rigid component dynamics used here is particularly suited to m = 1 perturbations like the hose instability, but with appropriate modifications this approach is applicable to m = 0 beam modes and possibly to other resonant instabilities of periodic systems.

We note that these hose stability results are restricted to beams propagating in a medium with a fixed conductivity profile. For the case of intense beams propagating into initially un-ionized or weakly ionized gas, the ionization and heating generated by the beam typically causes the conductivity channel to follow beam displacements. Since this effect reduces the separation between the beam and plasma currents, it is stabilizing. We have shown in the related case of the sausage instability[7] that this effect can be treated correctly only by including conductivity generation consistently in the equilibrium as well as in the perturbation, i.e. the equilibrium conductivity $\sigma(r,\zeta)$ must be allowed to increase with ζ. This self-consistent treatment of beam-generated conductivity introduces non-ignorable ζ dependence and is thus beyond the scope of the one-dimensional eigenvalue treatment developed in this paper. However, we have developed[8] a numerical treatment in which the multi-component model is solved by following the evolution of an initial perturbation in space and time, rather than by Fourier-analyzing in ζ and z. This approach allows us both to treat conductivity generation self-consistently and to include axial variations in the equilibrium beam and return currents. Since we do not assume high conductivity or charge neutrality in this time-dependent model, we can also treat the weakly-pinched beam head. This work will be reported in a separate publication.

It is also to be noted that in cases of very high beam current density and low enough background gas density, such as in ion beam transport for inertial confinement fusion, heating of the background gas can lead to significant hydrodynamic motion of the gas.[14] This effect should also be included self-consistently in a full treatment of hose instability in such systems.

Acknowledgments

We are grateful to Dr. Glenn Joyce, Dr. Richard F. Hubbard, and Dr. Adam T. Drobot for their sustained interest in this work.

The work was sponsored by the Defense Advanced Research Projects Agency (DOD) under ARPA Order No. 4395, Amendment No. 1.

Appendix A: Particle Orbit Properties

(i) Particle motion in the transverse plane

Usings the definitions (3)-(5), the energy H of a particle in a high-conductivity beam can be written in terms of the radial momentum component p_r and the canonical momentum components P_θ and P_z as

$$H \equiv \gamma Mc^2 = \left[M^2c^4 + c^2\left[p_r^2 + \frac{P_\theta^2}{r^2} + \left(P_z - \frac{q}{c} A_0\right)^2 \right]\right]^{1/2}. \tag{A1}$$

Equation (A1) may be regarded as an equation for p_r^2 as a function of r and the three constants of motion. For a paraxial beam with $p_z^2 >> p_r^2 + p_\theta^2$ and $v_z \approx c$,

$$|I_b| << I_A \equiv (\gamma^2-1)^{1/2} Mc^3 |q|^{-1}, \tag{A2}$$

and from Ampere's equation (2) we find

$$|qA_0/c| \lesssim |qI_b/c^2| << |qI_A/c^2| \approx \gamma Mc \approx p_z. \tag{A3}$$

This allows us to rewrite (A1) in the approximate form

$$H \approx \left[(\gamma_b Mc^2)^2 + c^2\left(p_r^2 + \frac{P_\theta^2}{r^2} - \frac{2qP_z}{c} A_0\right)\right]^{1/2}, \tag{A4}$$

where

$$\gamma_b Mc^2 \equiv \left(P_z^2c^2 + M^2c^4\right)^{1/2} \tag{A5}$$

is the energy associated with P_z. Since $\gamma_b Mc^2$ is large compared with the

energy in perpendicular motion and in A_0, (A4) can be approximated by

$$H \approx \gamma_b Mc^2 + \frac{1}{2\gamma_b M}\left(p_r^2 + \frac{P_\theta^2}{r^2}\right) - \frac{qP_z}{\gamma_b Mc} A_0. \tag{A6}$$

The radial velocity $v_r = p_r/(\gamma M) \approx p_r/(\gamma_b M)$ can then be written

$$v_r^2(r;H_\perp,P_\theta) \approx \frac{2}{\gamma_b M}\left[H_\perp - U(r;P_\theta)\right], \tag{A7}$$

where

$$H_\perp \equiv H - \gamma_b Mc^2, \tag{A8}$$

may be regarded as the energy in the transverse plane, and U is an effective potential given by

$$U(r;P_\theta) \equiv \frac{1}{2\gamma_b M}\frac{P_\theta^2}{r^2} - q\beta A_0(r). \tag{A9}$$

The complete particle dynamics thus reduces to motion in the transverse plane subject to an effective central potential.

(ii) Particle oscillation frequencies

Since v_r^2 is a function of r only, for a given $H_\perp$ and P_θ, particles execute periodic radial oscillations while gyrating at an angular velocity $\dot{\theta} = P_\theta/\gamma_b Mr^2$. The characteristic frequencies are the radial oscillation frequency

$$\Omega_r(H_\perp,P_\theta) = \pi\left[\int_{r_{min}}^{r_{max}} \frac{dr}{|v_r|}\right]^{-1} \tag{A10}$$

and the mean azimuthal frequency

$$\Omega_\theta(H_\perp,P_\theta) = \frac{\Omega_r(H_\perp,P_\theta)P_\theta}{\pi\gamma_b M} \int_{r_{min}}^{r_{max}} \frac{dr}{r^2|v_r|} \tag{A11}$$

where the turning points $r_{min}(H_\perp,P_\theta)$ and $r_{max}(H_\perp,P_\theta)$ are solutions of

$$v_r^2(r;H_\perp,P_\theta) = 0 \tag{A12}$$

such that $H_\perp > U(r;P_\theta)$ for $r_{min} < r < r_{max}$. In general, Ω_r/Ω_θ is irrational, and the orbits do not close. In the special case of a harmonic potential, corresponding to a uniform net current, these frequencies are independent of $H_\perp$ and P_θ, and $\Omega_r = 2\Omega_\theta$.

For particles confined near the axis, where the potential is nearly harmonic, we can express r_{min}, r_{max}, Ω_r, and Ω_θ in closed form. In this limit, the net current can be expanded in the form

$$J_{n0}(r) \approx J_{n0}(0)(1 - 2r^2/a_n), \tag{A13}$$

and $A_0(r)$ can be written to the same accuracy as

$$A_0(r) \approx -\frac{\pi}{c} J_{n0}(0)\, r^2\left(1 - \frac{r^2}{2a_n^2}\right), \tag{A14}$$

where a_n is the radial scale length of the net current profile and we assume

$$r^2/a_n^2 \ll 1, \tag{A15a}$$

which holds for particles with

$$H_\perp \ll q\beta A_0(a_n) \ . \tag{A15b}$$

Using (A14), we can reduce (A10) and (A11) to

$$\Omega_r = \pi\Omega_0\left(1 - \frac{r_{max}^2 + 2r_{min}^2}{2a_n^2}\right)^{1/2}\left[K\left(\frac{r_{max}^2 - r_{min}^2}{2a_n^2 - r_{max}^2 - 2r_{min}^2}\right)\right]^{-1} \tag{A16}$$

and

$$\Omega_\theta = \frac{\Omega_r}{\pi\Omega_0}\ \frac{a_n P_\theta}{\gamma_b M}\ \frac{2^{1/2}}{r_{min}^2\left(2a_n^2 - r_{max}^2 - 2r_{min}^2\right)^{1/2}}$$

$$\times\ \Pi\left(\frac{r_{min}^2 - r_{max}^2}{r_{min}^2},\ \frac{r_{max}^2 - r_{min}^2}{2a_n^2 - r_{max}^2 - 2r_{min}^2}\right), \tag{A17}$$

where $K(\alpha)$ and $\Pi(\alpha,\beta)$ are complete elliptic integrals of the first and third kinds[15],

$$\begin{aligned} K(\alpha) &\equiv \int_0^1 \frac{dx}{\left[(1-x^2)(1-\alpha x^2)\right]^{1/2}} \\ &\approx \frac{\pi}{2}\left(1 - \frac{1}{4}\,\alpha\right), \qquad \alpha \ll 1 \end{aligned} \tag{A18}$$

and

$$\Pi(\alpha,\beta) \equiv \int_0^1 \frac{dx}{(1-\beta x^2)[(1-x^2)(1-\alpha x^2)]^{1/2}}$$
$$\approx \frac{\pi}{2}\left[1+\left(\frac{1}{(1-\beta)^{1/2}} - 1\right)\frac{\alpha}{2\beta}\right], \qquad \alpha \ll 1 . \tag{A19}$$

In (A16) and (A17) we have introduced the characteristic frequency

$$\Omega_0 \equiv \left[\frac{2\pi q\beta}{\gamma_b M c} J_{n0}(0)\right]^{1/2},$$

and again $r_{min}(H_\perp, P_\theta)$ and $r_{max}(H_\perp, P_\theta)$ are defined by (A12). To zeroth order in r_{max}/a_n,

$$\begin{bmatrix} r_{max}^2 \\ r_{min}^2 \end{bmatrix} = \frac{H_\perp}{\gamma_b M \Omega_0^2}\left[1 \pm \left(1 - \frac{\Omega_0^2 P_\theta^2}{H_\perp^2}\right)^{1/2}\right]. \tag{A20}$$

Using this approximation and the small argument expansions of K and Π in (A18) and (A19), the orbit frequencies (A16) and (A17) can be rewritten as

$$\Omega_r \approx 2\Omega_0\left(1 - \frac{3H_\perp}{4\gamma_b M a_n^2 \Omega_0^2}\right) \tag{A21}$$

and

$$\Omega_\theta \approx \mathrm{sgn}(P_\theta)\Omega_0\left(1 - \frac{3H_\perp - \Omega_0|P_\theta|}{4\gamma_b M a_n^2 \Omega_0^2}\right). \tag{A22}$$

We see that Ω_0 is the magnitude of Ω_θ in the limit $H_\perp \to 0$.

In the opposite limit

$$r_{max}^2 / a_n^2 \gg 1, \tag{A23a}$$

which is equivalent to

$$H_\perp \gg q\beta A_0(a_n) , \tag{A23b}$$

we can make the approximation

$$A_0(r) \approx 4c^{-1} |I_n| \ln(r/a_n)$$

over most of a particle orbit. Writing $H_\perp$ in terms of the outer turning point $r_{max}(H_\perp,0)$ of a particle with $P_\theta = 0$, we then have

$$H_\perp - U(r;P_\theta) \approx \gamma_b M a_n^2 \Omega_0^2 \ln[r_{max}(H_\perp,0)/r] - \frac{1}{2\gamma_b M} \frac{P_\theta^2}{r^2} , \tag{A24}$$

and the orbit frequency expressions (A10) and (A11) reduce to

$$\Omega_r \approx \frac{\pi}{2^{1/2}} \frac{a_n \Omega_0}{r_{max}(H_\perp,0)} G_1\left(\frac{|P_\theta|}{\gamma_b M \Omega_0 a_n r_{max}(H_\perp,0)} \right), \tag{A25}$$

and

$$\Omega_\theta \approx \frac{a_n \Omega_0}{r_{max}(H_\perp,0)} G_2\left(\frac{|P_\theta|}{\gamma_b M \Omega_0 a_n r_{max}(H_\perp,0)} \right), \tag{A26}$$

where

$$G_1(y) \equiv \left[\int_{x_{min}}^{x_{max}} \frac{dx\, x}{(-2x^2 \ln x - y^2)^{1/2}} \right]^{-1}$$

$$G_2(y) \equiv y\, G_1(y) \int_{x_{min}}^{x_{max}} \frac{dx}{x(-2x^2 \ln x - y^2)^{1/2}} .$$

Here, $x_{min}(y)$ and $x_{max}(y)$ are the solutions of

$$- x^2 \ln x^2 = y^2. \tag{A27}$$

(iii) Density of the group of particles with the same Ω_θ

The group of particles with given Ω_θ includes particles with angular momentum P_θ ranging from zero for orbits through the axis to some maximum value for circular orbits. The orbit turning points likewise depend on P_θ, and in the small-orbit limit (A15), we can analytically calculate r_{max} as a function of Ω_θ and P_θ by combining (A20) and (A22). This procedure indicates that all particles with frequency Ω_θ are confined to the region $0 \leq r \leq \tilde{R}(\Omega_\theta)$, where

$$\tilde{R}^2(\Omega_\theta) = 3a_n^2(1-|\Omega_\theta|/\Omega_0) . \tag{A28}$$

Using this result, (A20) can be rewritten in the form

$$\begin{bmatrix} r_{max}^2 \\ r_{min}^2 \end{bmatrix} = \frac{2}{9} \tilde{R}^2[2 + S \pm 2(1 + S - 2S^2)^{1/2}], \tag{A29}$$

where

$$0 \leq S \equiv 9|P_\theta|/(8\gamma_b M\tilde{R}^2\Omega_0) \leq 1$$

We note that only particles with $S = 1/2$ and hence $|P_\theta| = 4\gamma_b M\tilde{R}^2\Omega_0/9$, pass through $\tilde{R}$, and the orbits of these particles are intermediate between radial ($P_\theta = 0$) and circular ($|P_\theta| = 8\gamma_b M\tilde{R}^2\Omega_0/9$). All other particles have $r_{max} < \tilde{R}$.

In the opposite limit (A23), we can rewrite (A26) as

$$r_{max}(H_\perp, P_\theta) = \frac{a_n\Omega_0}{|\Omega_\theta|} G_3\left(\frac{|P_\theta|}{\gamma_b M\Omega_0 a_n r_{max}(H_\perp, 0)} \right), \tag{A30}$$

where

$$G_3(y) \equiv x_{max}(y)\, G_2(y),$$

with x_{max} again given by (A27). The largest radius for a given value of Ω_θ is found by numerically calculating the maximum $G_3(y)$. This gives

$$\tilde{R}(\Omega_\theta) = 1.52\, a_n\Omega_0/|\Omega_\theta| \,. \tag{A31}$$

For intermediate $H_\perp$ values, $\tilde{R}(\Omega_\theta)$ must be calculated numerically, and the result for a beam with a Bennett profile (27) is shown in Fig. 2. We find for all $\tilde{R}$ values that particle orbits with $r_{max} = \tilde{R}(\Omega_\theta)$ are intermediate between circular and linear orbits.

When $J_{n0}(r)$ is peaked on-axis, so that Ω_θ is a monotonic function of $H_\perp$ for constant P_θ, the equilibrium beam current density (9) can be rewritten as

$$J_{b0}(r) = 2 \int_0^{\Omega_\theta(\tilde{R}=r)} d\Omega_\theta\, \delta J_0(r;\Omega_\theta), \tag{A32}$$

where

$$\delta J_0(r;\Omega_\theta) = \frac{2q\beta c}{r} \int_{P_{min}}^{P_{max}} dP_\theta \left| \frac{\partial H_\perp}{\partial \Omega_\theta} \right|_{P_\theta} \frac{F_0[H_\perp(\Omega_\theta,P_\theta)]}{|v_r(r;H_\perp,P_\theta)|} \tag{A33}$$

is the current density of particles with a given precession frequency Ω_θ. In (A33), P_{max} and P_{min} are the maximum and minimum P_θ values of particles with precession frequencies equal to Ω_θ and orbits passing through r.

In the small-orbit limit (A15), the density profile $\delta J_0(r;\Omega_\theta)$ can be calculated in closed form. To find the P_θ limits, we use (A22) to rewrite the turning point condition (A12) in the form

$$\frac{4}{3}\gamma_b M\Omega_0^2 a_n^2\left(1-\frac{|\Omega_\theta|}{\Omega_0}\right) - \frac{1}{2}\gamma_b M\Omega_0^2 r^2 + \frac{1}{3}\Omega_\theta|P_\theta| - \frac{P_\theta^2}{2\gamma_b M r^2} \approx 0 . \tag{A34}$$

We solve (A34) for $|P_\theta|$, and using (A28), we can write the solutions as

$$P_\pm(r;\Omega_\theta) = \frac{1}{3}\gamma_b M r^2\Omega_0 \left[1 \pm \left(8\frac{\tilde{R}^2(\Omega_\theta) - r^2}{r^2}\right)^{1/2}\right] . \tag{A35}$$

Since $|P_\theta|$ must be positive, we take $P_{max} = P_+$ and $P_{min} = \max(0,P_-)$, noting that P_{min} in (A33) is zero for

$$r^2 > \frac{8}{9}\tilde{R}^2(\Omega_\theta). \tag{A36}$$

For the Maxwell-Boltzmann distribution (64), we also have

$$F_0(H_\perp) \approx F_0(0) = J_{b0}(0)/(2\pi\gamma_b M q\beta c H_b) , \tag{A37}$$

to lowest order in r^2/a_n^2. The $\delta J_0(r;\Omega_\theta)$ expression (A33) can then be written

$$\delta J_0(r;\Omega_\theta) \approx \frac{16\beta}{3\pi}\frac{J_{b0}(0)}{\Omega_0}\int_{\max(0,P_-)}^{P_+}\frac{dP_\theta}{(P_+ - P_\theta)^{1/2}(P_\theta - P_-)^{1/2}}\ , \qquad \text{(A38)}$$

which gives

$$\delta J_0(r;\Omega_\theta) \approx \begin{cases} \delta J_0(0;\Omega_\theta)\left[1+\frac{2}{\pi}\sin^{-1}\left(\frac{1}{8}\frac{r^2}{\tilde{R}^2(\Omega_\theta)-r^2}\right)^{1/2}\right], & 0\le r^2\le \frac{8}{9}\tilde{R}^2(\Omega_\theta) \\ \delta J_0(0;\Omega_\theta)\ , & \frac{8}{9}\tilde{R}^2(\Omega_\theta)\le r^2\le \tilde{R}^2(\Omega_\theta) \\ 0\ , & \tilde{R}^2(\Omega_\theta) < r^2, \end{cases}$$

(A39)

where $\delta J_0(0;\Omega_\theta) = 8\beta J_{b0}(0)/(3\Omega_0)$. The profile (A39) is shown in Fig. 1. The discontinuity in δJ_0 that occurs at the outer radius $\tilde{R}$ is a general feature that has important consequences on the analytic structure of the eigenmodes.

Appendix B: Evaluation of the Vlasov Time Integral

In the Vlasov perturbed current expression (12), the accumulated effect of the wave on particles with some given $H_\perp$ and P_θ is expressed in terms of the time integral

$$I(r;H_\perp,P_\theta) = \frac{1}{2} \sum_{\pm} \int_{-\infty}^{z} dz' \, \hat{A}(r'_{\pm}) \exp\left[i(\theta'_{\pm} - \theta) - \frac{i\Omega}{\beta c}(z' - z)\right]. \qquad (B1)$$

Here, $z = \beta ct$ is a measure of propagation time, and r' and θ' are the unperturbed radial location and azimuthal angle at time $z' < z$ of particles with the specified $H_\perp$ and P_θ that reach the point (r,θ) at time z. The $\pm$ subscript indicates the sign of the radial velocity v_r at time z.

To put (B1) into a more useable form, we consider the change along the particle trajectories of the quantities

$$I_{\pm}(r,z) = \hat{I}[r_{\pm}(z)] \exp[i\phi_{\pm}(z)] = \int_{-\infty}^{z} dz' \, \hat{A}(r'_{\pm}) \exp(i\phi'_{\pm}) \, . \qquad (B2)$$

Here, the phase angle $\phi_{\pm}$ is defined by

$$\phi_{\pm}(z) = \theta_{\pm}(z) - \frac{\Omega}{\beta c} z, \qquad (B3)$$

and all orbit quantities are understood to depend on $H_\perp$ and P_θ. Since v_r and $\dot{\theta}$ are functions of r only for these particles, we can readily relate $I_{\pm}(r)$ to the values at the previous turning points:

$$\hat{I}_{+}(r) \exp(i\phi_{+}) = \hat{I}_{+}(r_{min}) \exp(i\phi^{+}_{min}) + \int_{r_{min}}^{r} dr' \exp(i\phi'_{+}) \qquad (B4a)$$

$$\hat{I}_-(r)\exp(i\phi_-) = \hat{I}_-(r_{max})\exp(i\phi^-_{max}) - \int_{r_{max}}^{r} d\Gamma' \exp(i\phi'_-), \qquad \text{(B4b)}$$

where r_{min} and r_{max} are the orbit turning points, and we have introduced the compact notation

$$\phi^+_{min} \equiv \phi_+(r_{min}) = \phi_+(r) - \int_{r_{min}}^{r} \frac{dr'}{|v_r(r')|}\left[\dot{\theta}(r') - \Omega\right], \qquad \text{(B5a)}$$

$$\phi^-_{max} \equiv \phi_-(r_{max}) = \phi_-(r) + \int_{r_{max}}^{r} \frac{dr'}{|v_r(r')|}\left[\dot{\theta}(r') - \Omega\right], \qquad \text{(B5b)}$$

and

$$d\Gamma' \equiv \frac{dr'}{|v_r(r')|}\beta c\hat{A}(r'). \qquad \text{(B5c)}$$

We eliminate ϕ_- from (B4) by noting first that

$$\phi_+(r) - \phi^+_{min} = -\left[\phi_-(r) - \phi_-(r_{min})\right]. \qquad \text{(B6)}$$

The relative phase between ϕ_+ and ϕ_- is fixed by taking the phase angles to be equal at r_{min}, so that $\phi_-(r_{min}) = \phi^+_{min} \equiv \phi_{min}$. We then rewrite (B6) as

$$\phi_-(r) = 2\phi_{min} - \phi_+(r) \qquad \text{(B7)}$$

and substitute this expression for ϕ_- in (B4).

The turning point values $\hat{I}^+_{min} \equiv \hat{I}_+(r_{min})$ and $\hat{I}^-_{max} \equiv \hat{I}_-(r_{max})$ are determined by evaluating the full change in $\hat{I}_\pm$ between turning points:

$$\hat{I}^{+}_{max}\exp(i\phi^{+}_{max}) - \hat{I}^{+}_{min}\exp(i\phi_{min}) = \int_{r_{min}}^{r_{max}} dr'\exp(i\phi'_{+}) \tag{B8a}$$

$$\hat{I}^{-}_{min}\exp(i\phi_{min}) - \hat{I}^{-}_{max}\exp[i(2\phi_{min} - \phi^{+}_{max})] = \int_{r_{min}}^{r_{max}} dr'\exp[i(2\phi_{min} - \phi'_{+})]. \tag{B8b}$$

Since the continuity of particle orbits gives $\hat{I}^{+}_{min} = \hat{I}^{-}_{min} \equiv \hat{I}_{min}$ and $\hat{I}^{+}_{max} = \hat{I}^{-}_{max} \equiv \hat{I}_{max}$, (B9) can be solved for $\hat{I}_{min}$ and $\hat{I}_{max}$:

$$\hat{I}_{min} = \frac{D_{+}\exp(-i\Delta\phi) + D_{-}\exp(i\Delta\phi)}{\exp(i\Delta\phi) - \exp(-i\Delta\phi)} \tag{B9a}$$

$$\hat{I}_{max} = \frac{D_{+} + D_{-}}{\exp(i\Delta\phi) - \exp(-i\Delta\phi)} \ , \tag{B9b}$$

where

$$D_{\pm} \equiv \int_{r_{min}}^{r_{max}} dr'\exp[\pm i(\phi'_{+} - \phi_{min})]$$

and

$$\Delta\phi \equiv \phi^{+}_{max} - \phi^{+}_{min} = \int_{r_{min}}^{r_{max}} \frac{dr'}{|v_r(r')|}\,[\dot{\theta}(r') - \Omega] = \pi\,\frac{\Omega_\theta - \Omega}{\Omega_r} \ .$$

We substitute (B9) into (B4) to obtain expressions for $\hat{I}_{\pm}(r)$ in terms only of orbit integrals from r_{min} to $r \leq r_{max}$. Suppressing the superfluous + subscript on ϕ, we find

$$\hat{I}_+(r) = \int_{r_{max}}^{r} d\Gamma' \exp[i(\phi' - \phi)]$$

$$+ \frac{1}{2i \sin(\Delta\phi)} \int_{r_{min}}^{r_{max}} d\Gamma' \{\exp[i(\phi' - \phi - \Delta\phi)] + \exp[-i(\phi' + \phi - \Delta\phi)]\} \qquad \text{(B10a)}$$

and

$$\hat{I}_-(r) = \int_{r_{min}}^{r_{max}} d\Gamma' \exp[-i(\phi' - \phi)]$$

$$+ \frac{\exp(-i\Delta\phi)}{2i \sin(\Delta\phi)} \int_{r_{min}}^{r_{max}} d\Gamma' \{\exp[i(\phi' + \phi)] + \exp[-i(\phi' - \phi)]\}. \qquad \text{(B10b)}$$

Since $\hat{I}(r) = \frac{1}{2}[\hat{I}_+(r) + \hat{I}_-(r)]$, we can combine these $\hat{I}_{\pm}$ expressions into

$$\hat{I}(r) = \frac{1}{2} \int_{r_{min}}^{r_{max}} d\Gamma' \{\exp[i \, \mathrm{sgn}(r-r') \, (\phi' - \phi)]$$

$$- \frac{i}{\sin(\Delta\phi)} [\exp(-i\Delta\phi)\cos(\phi' - \phi) + \cos(\phi' + \phi - \Delta\phi)]\} . \qquad \text{(B11)}$$

When the exponentials and cosines in (B11) are expanded, some cancellations occur, and we obtain the more compact form

$$\hat{I}(r) = -i\beta c \int_{r_{min}}^{r_{max}} \frac{dr'}{|v_r(r')|} \hat{A}(r')$$

$$\times \left[\frac{\cos\phi\cos\phi'}{\tan(\Delta\phi)} + \Theta(r-r')\sin\phi\cos\phi' + \Theta(r'-r)\sin\phi'\cos\phi \right] , \qquad \text{(B12)}$$

where Θ is the unit step function and (B5c) has been substituted for $d\Gamma'$. This form of $\hat{I}$ can conveniently be used either to evaluate $\hat{J}(r)$ numerically or to investigate its analytic properties.

References

1. M. N. Rosenbluth, Phys. Fluids 3, 932 (1960).
2. E. P. Lee and L. D. Pearlstein, Phys. Fluids 16, 904 (1973).
3. S. Weinberg, J. Math, Phys. 5, 1371 (1964).
4. S. Weinberg, J. Math, Phys. 8, 614 (1967).
5. E. P. Lee, Phys. Fluids 21, 1327 (1978).
6. H. S. Uhm and M. Lampe, Phys. Fluids 23, 1574 (1980).
7. M. Lampe, W. M. Sharp, G. Joyce, R. F. Hubbard, and H. S. Uhm, in Proceedings of The Fourth International Conference on High Power Electron and Ion Beam Research and Technology, Ecole Polytechnique, Palaiseau, France, June 1981.
8. R. F. Hubbard, G. Joyce, M. Lampe, W. M. Sharp, and S. P. Slinker, Bull. Am. Phys. Soc. 26, 915 (1981).
9. W. M. Sharp and M. Lampe, Phys. Fluids 23, 2383 (1980).
10. E. P. Lee, Lawrence Livermore National Laboratory Report UCID-18768 (1980).
11. W. H. Bennett, Phys. Rev. 45, 890 (1934).
12. J. H. Wilkinson, The Algebraic Eigenvalue Problem (Clarendon Press, Oxford, 1965), p. 322.
13. H. S. Uhm and M. Lampe, Phys. Fluids 24, 1553 (1981).
14. D. G. Colombant, S. A. Goldstein, and D. Mosher, Phys. Rev. Lett. 45, 1253 (1980).
15. M. Abramowitz and I. A. Stegun, Eds., Handbook of Mathematical Functions (National Bureau of Standards, Washington, D.C., 1967), pp. 589-607.

DISTRIBUTION LIST

1. Commander
   Naval Sea Systems Command
   Department of the Navy
   Washington, D.C. 20363
   Attn: NAVSEA 03H (Dr. C. F. Sharn)

2. Central Intelligence Agency
   P.O. Box 1925
   Washington, D.C. 20013
   Attn: Dr. C. Miller/OSI

3. Air Force Weapons Laboratory
   Kirtland Air Force Base
   Albuquerque, New Mexico 87117
   Attn: Lt. Col. J. H. Havey

4. U. S. Army Ballistics Research Laboratory
   Aberdeen Proving Ground, Maryland 21005
   Attn: Dr. D. Eccleshall (DRXBR-BM)

5. Ballistic Missile Defense Advanced Technology Center
   P.O. Box 1500
   Huntsville, Alabama 35807
   Attn: Dr. L. Havard (BMDSATC-1)

6. B-K Dynamics, Inc.
   15825 Shady Grove Road
   Rockville, Maryland 20850
   Attn: Mr. I. Kuhn

7. Intelcom Rad Tech.
   P.O. Box 81087
   San Diego, California 92138
   Attn: Mr. W. Selph

8. Lawrence Livermore National Laboratory
   University of California
   Livermore, California 94550
   Attn: Dr. R. J. Briggs
   Dr. T. Fessenden
   Dr. E. P. Lee
   Dr. F. Chambers
   Dr. S. Yu
   Dr. James W.-K. Mark, L-477
   Dr. W. Fauley
   Dr. H. L. Buchanon
   Dr. J. Masamitsu
   Dr. W. Barletta

9. Mission Research Corporation
735 State Street
Santa Barbara, California 93102
Attn: Dr. C. Longmire
Dr. N. Carron

10. National Bureau of Standards
Gaithersburg, Maryland 20760
Attn: Dr. Mark Wilson

11. Science Applications, Inc.
1200 Prospect Street
La Jolla, California 92037
Attn: Dr. M. P. Fricke
Dr. W. A. Woolson

12. Science Applications, Inc.
5 Palo Alto Square, Suite 200
Palo Alto, California 94304
Attn: Dr. R. R. Johnston
Dr. Leon Feinstein

13. Science Applications, Inc.
1651 Old Meadow Road
McLean, Virginia 22101
Attn: Mr. W. Chadsey

14. Science Applications, Inc.
8201 Capwell Drive
Oakland, California 94621
Attn: Dr. J. E. Reaugh

15. Naval Surface Weapons Center Detachment
White Oak Laboratory
Silver Spring, Maryland 20910
Attn: Mr. R. J. Biegalski
Dr. R. Cawley
Dr. J. W. Forbes
Dr. D. L. Love
Dr. C. M. Huddleston
Dr. G. E. Hudson
Mr. W. M. Hinckley
Mr. N. E. Scofield
Dr. E. C. Whitman
Dr. M. H. Cha
Dr. H. S. Uhm
Dr. R. Fiorito

16. C. S. Draper Laboratories
Cambridge, Massachusetts 02139
Attn: Dr. E. Olsson
Dr. L. Matson

17. M.I.T. Lincoln Laboratories
P.O. Box 73
Lexington, Massachusetts 02173
Attn: Dr. J. Salah

18. Physical Dynamics, Inc.
P.O. Box 1883
La Jolla, California 92038
Attn: Dr. K. Brueckner

19. Office of Naval Research
Department of the Navy
Arlington, Virginia 22217
Attn: Dr. W. J. Condell (Code 421)

20. Avco Everett Research Laboratory
2385 Revere Beach Pkwy
Everett, Massachusetts 02149
Attn: Dr. R. Patrick
Dr. Dennis Reilly
Dr. D. H. Douglas-Hamilton

21. Defense Technical Information Center
Cameron Station
5010 Duke Street
Alexandria, VA 22314 (2 copies)

22. Naval Research Laboratory
Washington, D.C. 20375
Attn:
M. Lampe - Code 4792 (50 copies)
M. Friedman - Code 4700.1
J. R. Greig - Code 4763
I. M. Vitkovitsky - Code 4770
J. B. Aviles - Code 4665
M. Haftel - Code 4665
T. Coffey - Code 4000
Superintendent, Plasma Physics Div. - Code 4700 (26 copies)
P. Sprangle - Code 4790
Library - Code 2628 (20 copies)
A. Ali - Code 4700.1
D. Book Code 4040
J. Boris - Code 4040
I. Haber - Code 4790
B. Hui - Code 4790
S. Kainer - Code 4790
G. Joyce - Code 4790
D. Murphy - Code 4763
A. Robson - Code 4760
D. Colombant - Code 4790
M. Picone - Code 4040
M. Raleigh - Code 4760
R. Pechacek - Code 4763

23. Defense Advanced Research Projects Agency
1400 Wilson Blvd.
Arlington, VA 22209
Attn: Dr. J. Mangano
Dr. J. Bayless

24. JAYCOR
5705A General Washington Drive
Alexandria, VA 22312
Attn: Dr. D. Tidman
Dr. R. Hubbard
Dr. J. Guillory
Dr. S. Slinker

25. JAYCOR
Naval Research Laboratory
Washington, D.C. 20375
Attn: Dr. R. Fernsler - Code 4763
Dr. S. Goldstein - Code 4770

26. SAI
Naval Research Laboratory
Washington, D.C. 20375
Attn: A. Drobot - Code 4790
W. Sharp - Code 4790

27. Physics International, Inc.
2700 Merced Street
San Leandro, CA.
Attn: Dr. E. Goldman

28. Mission Research Corp.
1400 San Mateo, S.E.
Albuquerque, NM 87108
Attn: Dr. Brendan Godfrey

29. Princeton University
Plasma Phvsics Laboratory
Princeton, NJ 08540
Attn: Dr. Francis Perkins, Jr.

30. McDonnell Douglas Research Laboratories
Dept. 223, Bldg. 33, Level 45
Box 516
St. Louis, MO 63166
Attn: Dr. Michael Greenspan

31. Cornell University
Ithaca, NY 14853
Attn: Prof. David Hammer

32. Sandia Laboratories
Albuquerque, NM 87185
Attn: Dr. Bruce Miller
Dr. Barbara Epstein
Dr. John Freeman

33. University of California
Physics Department
Irvine, CA 92717
Attn: Dr. Gregory Benford

34. Beers Associates Inc.
Att: Dr. Douglas Strickland
P.O. Box 2549
Reston Va. 22090

35. Air Force Weapons Laboratory
Kirtland Air Force Base
Albuquerque, NM 87117
Attn:
D. Straw (AFWL/NTYP)
R. Lemke (AFWL/NTYP)
C. Clark (AFWL/NTYP)
W. Baker (AFWL/NTYP)

36. R&D Associates
P.O. Box 9695
Marina del Rey, CA 90291

37. Pulse Sciences, Inc.
1615 Broadway - Suite 610
Oakland, CA 94612
Attn: Dr. Sidney Putman

38. Los Alamos National Scientific Laboratory
P.O. Box 1663
Los Alamos, NM 87545
Attn: Dr. L. Thode
Dr. A. B. Newberger, X-3, MS-608
Dr. M. A. Mostrom, MS-608
Dr. T. P. Starke
Dr. H. Dogliani

39. Western Research Corp
8616 Commerce Ave.
San Diego, CA 92121
Attn: Dr. Frank Felber

40. Dr. J. M. Dolique
Laboratoire de Physique des Plasmas
Universite' de Grenoble I
B.P. 53X
38041 Grenoble Cedex
FRANCE

41. CEN Saclay
D.P.C. Bab 22
B.P. No. 2
91191 Gif-sur-Yvette
FRANCE
Attn: Dr. Babuel-Peyrissac

42. University of Maryland
Physics Department
College Park, MD 20742
Attn: Dr. Y. C. Lee
Dr. C. Grebogi

43. Rutherford Laboratory
Chilton, Didcot
Oxon OX11 0QX
United Kingdom
Attn: Dr. D. V. Bugg

44. Karacsony Fanos
Center for Theoret. Physics
University of Cluj
3.400 CLUJ-NAPOCA
ROMANIA

45. Maxwell Laboratories, Inc.
8835 Balboa Ave.
San Diego, CA 92123
Attn: Dr. Nino Pereira

46. Fraunhofer-Gesellschaft
Institut fur Naturwissenschaftlich-Technische Trendanalysen (INT)
Appelsgarten 2
5350 Euskirchen/Rhld.
West-Germany
Attn: Dr. A. Knoth

47. Dr. A. S. Paithankar
Bhabha Atomic Research Centre
Electronics & Instrumentation Group,
Plasma Physics Section
PRIP Shed. Trombay
Bombay-400 085. INDIA